Cell Metabolism

Quantitative Analysis of NAD Synthesis-Breakdown Fluxes

Graphical Abstract

Highlights

- Isotope-tracer methods reveal NAD sources and sinks, quantitatively

- Liver makes NAD from tryptophan, excreting nicotinamide for use by other tissues

- NAD fluxes vary widely across tissues ($t_{1/2}$ 15 min to 15 hr)

- Intravenous, but not oral, nicotinamide riboside is delivered intact to tissues
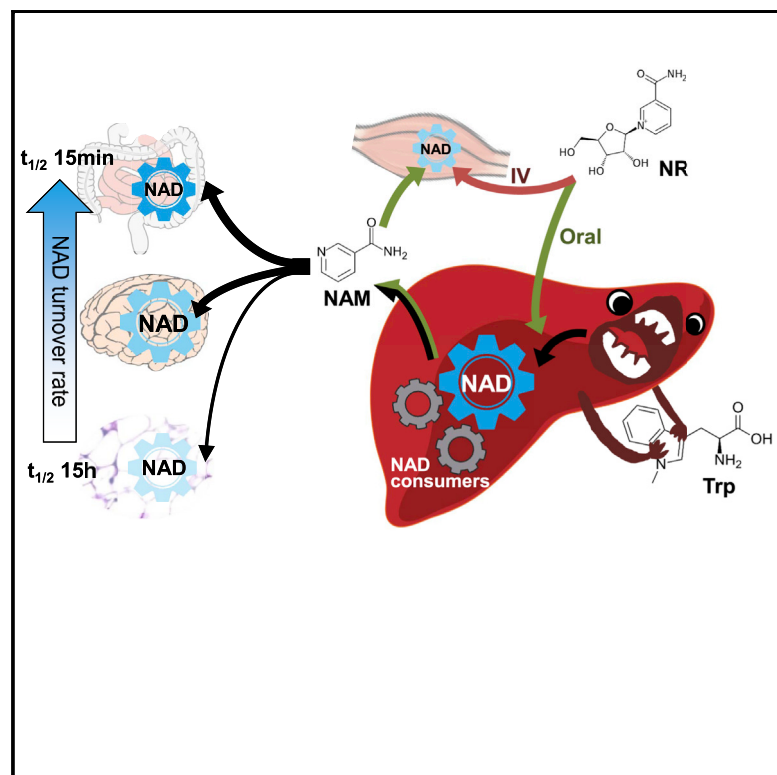
Authors

Ling Liu, Xiaoyang Su,
William J. Quinn III, ...,
Timothy J. Mitchison, Joseph A. Baur,
Joshua D. Rabinowitz

Correspondence

timothy_mitchison@hms.harvard.edu
(T.J.M.),
baur@mail.med.upenn.edu (J.A.B.),
joshr@princeton.edu (J.D.R.)

In Brief

Tissue concentrations of the redox cofactor NAD change during aging and disease. Liu et al. developed isotope-tracer methods to quantitate NAD fluxes in cell culture and in mice, revealing that the liver makes NAD from tryptophan and from orally delivered nicotinamide riboside, a nutraceutical. In contrast, other tissues rely on circulating nicotinamide for NAD synthesis.

CellPress

Article

Quantitative Analysis of NAD Synthesis-Breakdown Fluxes

Ling Liu,[1,2,3] Xiaoyang Su,[1,4] William J. Quinn III,[5] Sheng Hui,[1] Kristin Krukenberg,[6,7] David W. Frederick,[5] Philip Redpath,[8] Le Zhan,[9] Karthikeyani Chellappa,[5] Eileen White,[9] Marie Migaud,[8,10] Timothy J. Mitchison,[6,*] Joseph A. Baur,[5,*] and Joshua D. Rabinowitz[1,2,3,11,*]

[1]Lewis-Sigler Institute for Integrative Genomics, Princeton University, Princeton, NJ 08540, USA
[2]Department of Chemistry, Princeton University, Princeton, NJ 08540, USA
[3]Diabetes Research Center, University of Pennsylvania, Philadelphia, PA 19104, USA
[4]Department of Medicine, Robert Wood Johnson Medical School, Rutgers University, New Brunswick, NJ 08904, USA
[5]Department of Physiology and Institute for Diabetes, Obesity, and Metabolism, Perelman School of Medicine, University of Pennsylvania, Philadelphia, PA 19104, USA
[6]Department of System Biology, Harvard Medical School, Boston, MA 02115, USA
[7]Shire, Lexington, MA 02421, USA
[8]School of Pharmacy, Queen's University Belfast, Belfast, Northern Ireland BT9 7BL, UK
[9]Rutgers Cancer Institute of New Jersey, New Brunswick, NJ 08903, USA
[10]Mitchell Cancer Institute, University of South Alabama, Mobile, AL 36604, USA
[11]Lead Contact
*Correspondence: timothy_mitchison@hms.harvard.edu (T.J.M.), baur@mail.med.upenn.edu (J.A.B.), joshr@princeton.edu (J.D.R.)
https://doi.org/10.1016/j.cmet.2018.03.018

SUMMARY

The redox cofactor nicotinamide adenine dinucleotide (NAD) plays a central role in metabolism and is a substrate for signaling enzymes including poly-ADP-ribose-polymerases (PARPs) and sirtuins. NAD concentration falls during aging, which has triggered intense interest in strategies to boost NAD levels. A limitation in understanding NAD metabolism has been reliance on concentration measurements. Here, we present isotope-tracer methods for NAD flux quantitation. In cell lines, NAD was made from nicotinamide and consumed largely by PARPs and sirtuins. *In vivo*, NAD was made from tryptophan selectively in the liver, which then excreted nicotinamide. NAD fluxes varied widely across tissues, with high flux in the small intestine and spleen and low flux in the skeletal muscle. Intravenous administration of nicotinamide riboside or mononucleotide delivered intact molecules to multiple tissues, but the same agents given orally were metabolized to nicotinamide in the liver. Thus, flux analysis can reveal tissue-specific NAD metabolism.

INTRODUCTION

The redox cofactor NAD (nicotinamide adenine dinucleotide) plays a central role in cellular energy generation, carrying high-energy electrons and driving oxidative phosphorylation (Pollak et al., 2007). NAD is regenerated from NADH by oxidation, with rapid cycling between the oxidized and reduced forms. The total pool size of NAD(H) depends on the relative rates of synthesis and degradation. In mammals, NAD is made *de novo* from tryptophan, via the Preiss-Handler pathway from nicotinic acid (NA), via the salvage pathway from nicotinamide (NAM, the redox-active ring alone, without ADP-ribose), or via the nicotinamide ribose kinase pathway from nicotinamide riboside (NR) (Hassa et al., 2006; Bogan and Brenner, 2008; Mori et al., 2014). NAD is consumed by NAD kinase, which makes the anabolic and redox defense cofactor NADP(H), as well as multiple families of signaling enzymes. Sirtuins (SIRTs) remove acyl marks (most commonly acetylation) on proteins using NAD, generating O-acyl-ADP-ribose and NAM (Haigis and Sinclair, 2010). ADP-ribosyl-transferases, most famously poly-ADP-ribose-polymerases (PARPs), which play an important role in DNA damage repair, use NAD to modify proteins with ADP-ribosyl groups (Rouleau et al., 2010). Cyclic ADP-ribose hydrolases (CD38/CD157) consume NAD to make the calcium-releasing second messengers, cyclic ADP-ribose and NAADP (Malavasi et al., 2008). Puzzlingly, the catalytic domain of CD38 faces the extracellular space under normal conditions, raising questions of how it accesses NAD (Zhao et al., 2015). Thus, NAD metabolism is complex, with multiple production routes and a myriad of consuming enzymes, many of which primarily function in signaling, rather than metabolism.

Measuring NAD metabolism is of great interest due to NAD's fundamental biological importance, and ties to human disease and normal aging. NAD is gradually depleted during aging in multiple tissues and has been proposed as a master regulator of age-dependent pathology (Chini et al., 2017). Its depletion induces mitochondrial dysfunction and nuclear DNA damage by mechanisms that are currently under intense investigation (Fang et al., 2016; van de Ven et al., 2017). Acute NAD depletion has been proposed to promote neurodegeneration, to drive cardiomyocyte damage during heart attacks, and to potentiate the killing of cancer cells by chemotherapy (Hasmann and Schemainda, 2003).

Consistent with the medical importance of NAD metabolism, there has been great interest in its pharmacological modulation.

Small-molecule PARP inhibitors promote cell death in certain cancers by blocking DNA damage repair (Davar et al., 2012), but also spare NAD, which can be beneficial in other settings (Pirinen et al., 2014; Fang et al., 2014). Hyperactivation of PARPs promotes cell death through multiple mechanisms, including NAD depletion and signaling through PAR-dependent pathways (Virág et al., 2013; Fouquerel et al., 2014). Inhibitors of the enzyme NAMPT, which is required for NAD biosynthesis from NAM, are in clinical trials for cancer treatment, based on their potential to deplete NAD and thereby block cancer growth (Chini et al., 2014). Certain cancers cannot make NAD from NA, which led to the concept of rescuing normal cells, but not vulnerable cancer cells, from NAMPT inhibition using NA (Xiao et al., 2013). NAMPT activators are under investigation for treating neurodegeneration by raising NAD (Wang et al., 2005, 2014). Activators of NAD-consuming SIRTs, whose activities are suspected to deleteriously drop when NAD levels are low in aging and degenerative disease, have also been proposed as therapeutics (Bonkowski and Sinclair, 2016). CD38 deletion is effective in reducing diet-induced obesity and metabolic syndrome in mouse models, and is thought to act in part by increasing tissue NAD levels (Chini, 2009). Finally, there is extensive interest in NR and NMN, which can be converted into NAD without passing through the gating enzyme for NAM assimilation, NAMPT, as nutraceuticals to boost NAD levels and prevent the effects of aging (Ryu et al., 2016; Trammell et al., 2016).

To date, analysis of NAD metabolism and related drug perturbations has largely relied on measurement of the concentration of NAD, and occasionally of related metabolites, and on how these levels change in response to drug perturbation, disease, and aging. In addition, enzyme activities in lysates have been measured (Mori et al., 2014). Estimating NAD synthesis and breakdown rates based on concentrations or biochemical assays is insufficient: an increased concentration may reflect increased production or decreased consumption, while enzyme activities in lysates may not reflect cellular regulatory mechanisms. Accordingly, there is an unmet need to measure NAD production and consumption rates in cells and tissues (fluxes). Flux measurement holds the potential to illuminate the main pathways responsible for NAD production and consumption, and how they differ across cell types, tissues, and disease states. Although ^{14}C tracing to estimate NAD turnover was reported more than 40 years ago (Hillyard et al., 1973; Rechsteiner et al., 1976a, 1976b; Ijichi et al., 1966; Hayaishi et al., 1967), mass spectrometry now allows similar experiments to be conducted using stable isotopes, with quantitative measurement of both unlabeled and labeled forms of different NAD-related metabolites (Trammell and Brenner, 2013; Ratajczak et al., 2016).

Here, we establish methods for measurement of NAD synthesis and breakdown fluxes in cell lines and mouse tissues using stable isotope tracers combined with mathematical modeling. We find that NAM is the main NAD source in both cell lines and most murine tissues. Liver actively makes NAD *de novo* from tryptophan, releasing NAM into the blood, which supports NAD biosynthesis in the rest of the body. Mouse tissues vary markedly in NAD fluxes and turnover rates, with the liver, lung, spleen, and small intestine having a faster turnover half-time than any of the tested cultured cell lines, and the skeletal muscle slower. Unlike in cell culture, where NR and NMN are readily incorporated into NAD (Ratajczak et al., 2016; Frederick et al., 2016), oral administration fails to deliver NR or NMN to tissues without breaking the nicotinamide-ribose bond. Assimilation after intravenous (i.v.) administration varies between tissues, with NR being used preferentially over NMN in the muscle. Future pharmacological and nutraceutical efforts to boost NAD will need to take into account the minimal oral bioavailability of NR and NMN and the tissue-specific features of NAD metabolism.

RESULTS

NAD Flux Quantification

To quantify NAD metabolism in tissue culture, we substituted [2,4,5,6-^{2}H]NAM into the media of T47D breast cancer cells. DMEM with 10% dialyzed serum was prepared from scratch with solely isotopic NAM (32 μM, the standard DMEM concentration, which is 15× normal circulating levels in mice; Table S1) (Figure 1A). Feeding-labeled NAM resulted, at steady state, in nearly complete NAD labeling. Feeding [U-^{13}C]Trp did not result in detectable NAD labeling, even after 4 days in NAM-free medium (Figures S1A and S1B), consistent with lack of the relevant enzyme expression in T47D cells (Schreiber et al., 2006; Xiao et al., 2013). There is no NA or NR in standard cell culture medium. Thus, in these typical cell culture conditions, essentially all NAD is synthesized from NAM.

Figure 1A schematizes NAD synthesis and breakdown fluxes at steady state in growing cells; f_{in} is the synthetic flux from NAM to NAD, f_{growth} accounts for dilution by growth, and f_{out} accounts for the collective breakdown by NAD kinase, PARPs, etc. Color indicates isotope labeling following transfer into isotope-labeled medium. Dynamic labeling studies revealed that labeling of intracellular NAM ($t_{1/2}$ 20 min) was much faster than that of NAD ($t_{1/2}$ 9 hr) (Figure 1B). Thus, NAM equilibration across the membrane is fast compared with NAD biosynthesis.

Switching to labeled NAM did not alter the NAD concentration (Figure S1C). Although the NAM was M+4, most labeled NAD was M+3, as expected due to rapid turnover of the redox-active hydrogen at the 4 position (Figure 1C). The observed rate of NAD M+3 production may be slowed by the deuterium kinetic isotope effect at the redox-active hydrogen position. Nevertheless, the oxidation-reduction cycle between NAD and NADH is sufficiently rapid so as to result in the indistinguishable labeling kinetics for NAD and NADH (Figure S1D). Thus, we approximate NAD(H) as a single well-mixed pool for the purposes of the NAD-tracing studies reported here. Neither the deuterium at the 4 position nor the other deuterium-labeled sites are involved in the NAD synthesis and consumption reactions that we study, and thus are not expected to impact the fluxes that we measure.

In addition to NAD M+4 and M+3, we also observed a minor NAD M+2 fraction (Figure 1D). The M+2 species could, in theory, arise from interconversion between NAD and quinolinic acid, or spontaneous hydrogen-deuterium exchange. RNAi knockdown of quinolinate phosphoribosyl transferase did not inhibit formation of the M+2 species, suggesting it is generated by spontaneous exchange (Buncel and Lee, 1976) (Figures S1E and S1F).

We next developed a quantitative analysis of the fluxes underlying the observed labeling dynamics. After being taken up by cells, NAM forms NAD with flux f_{in}. In the presence of labeled
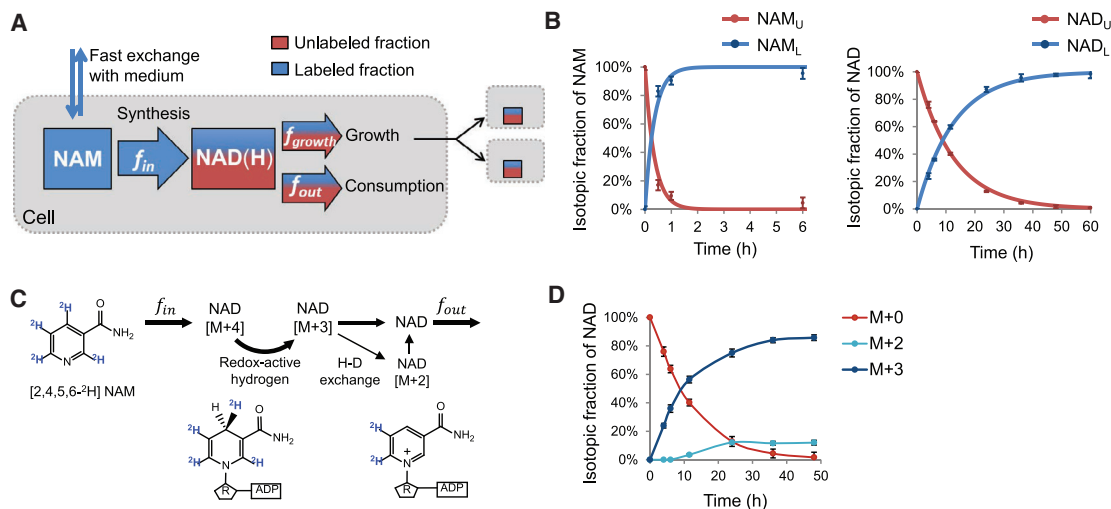
Figure 1. Quantitation of NAD Turnover in Cell Culture

(A) Switching the media from unlabeled to [2,4,5,6-^{2}H]nicotinamide, [^{2}H]NAM, results in NAD labeling without otherwise perturbing cellular pool sizes or fluxes. Fast labeling implies high fluxes relative to pool size.

(B) Isotopic fractions of intracellular NAM and NAD after switching to [^{2}H]NAM in T47D cells; U, unlabeled fraction; L, labeled fraction.

(C) Labeling schematic.

(D) NAD labeling dynamics after switching to [^{2}H]NAM in T47D cells.

Symbols, experimental data (mean ± SD, n = 3); lines are to guide the eye.

See also Figure S1 and Table S1.

NAM, the unlabeled fraction of NAD (NAD$_U$) (Figure 1B) accordingly decreases:

$$\frac{dNAD_U}{dt} = -\frac{f_{in}}{[NAD]}NAD_U \qquad \text{(Equation 1)}$$

[NAD] is the constant total intracellular concentration of NAD(H) (i.e., the sum of the oxidized and reduced cofactor concentrations, which is 1,880 pmol per million cells, with [NAD] > [NADH]; note that the volume of 1 million cells is about 3 μL, so this equates to about 0.6 mM NAD). Based on the experimental data for isotope incorporation (Figures 1B and 1C), f_{in} is 144 pmol per million cells per hr, with a 95% confidence interval (CI) of 121–169 (determined by bootstrapping). The NAD synthesis flux f_{in} must balance with (1) all NAD consumption (i.e., due to PARPs, SIRTs, CD38, NAD kinase, and other NAD-consumers, the sum of which is f_{out}) and (2) expansion of the NAD pool due to cell growth (f_{growth}). Cell growth was measured separately to determine the growth rate constant (g) with $f_{growth} = g$ [NAD]. In T47D cells, f_{growth} accounts for ∼20% of f_{in}. Therefore, with the NAD concentration of about 0.6 mM, and a turnover t$_{1/2}$ of 9 hr, T47D cells break down a majority of newly made NAD.

NAD Consumption Routes

NAD is the substrate for essential metabolic processes including NADP synthesis by NAD kinase and important protein covalent modification reactions (e.g., deacetylation and ADP-ribosylation). We sought to separately quantify the major NAD-consuming pathways (Figure 2A). To investigate the contribution of NAD kinase, we measured the dynamics of NADP labeling. Like NAD/NADH, NADP/NADPH are coupled by rapid oxidation-reduction and label equally (Figure S1D).

Compared with NAD, NADP labeled detectably more slowly (Figure 2B). The slower labeling does not reflect a slower intrinsic turnover rate of NADP(H) relative to NAD(H), but rather the NADP being downstream of NAD, with the time lag in labeling used to calculate the NAD kinase forward flux (f_1) (Yuan et al., 2008) (STAR Methods). Based on the labeling kinetics, the intrinsic turnover half-time of NADP is about 2-fold shorter than for NAD. However, due to the 20-fold smaller total pool size of NADP(H) relative to NAD(H) (Figure S1G), the NAD kinase flux is only ∼10% of total NAD consumption, 12 pmol per million cells per hr (CI: 11–14), compared with total NAD consumption of 118 pmol per million cells per hr.

To measure NAD consumption by PARP1/2, the major DNA damage responsive PARPs, we switched exponentially growing cells simultaneously into [^{2}H]NAM and olaparib (AZD2281), an FDA-approved PARP1/2 inhibitor drug (Menear et al., 2008). Compared with untreated cells, olaparib-treated cells accumulated an indistinguishable amount of labeled NAD at early time points (Figure 3A, blue lines), indicating that NAD synthesis from NAM is unaltered. The decay of unlabeled NAD was, however, slower, resulting in an approximately 10% increase in NAD concentration over 15 hr. Thus, PARP inhibition increased the NAD pool by decreasing its consumption (Nikiforov et al., 2011). Based on the slower rate of unlabeled NAD decline, we determined the value of f_{out} upon inhibitor treatment (Figures 3B and 3C) to be 79 pmol per million cells per hr (versus 118 in the absence of PARP inhibition), with the difference being the PARP contribution of 39 pmol per million cells per hr (CI: 28–43). A caveat is that this calculation assumes constant NAD consumption by other pathways, whereas the rise in total NAD concentration after inhibitor treatment could be driving compensatory increases in other components of f_{out}. Due to the small
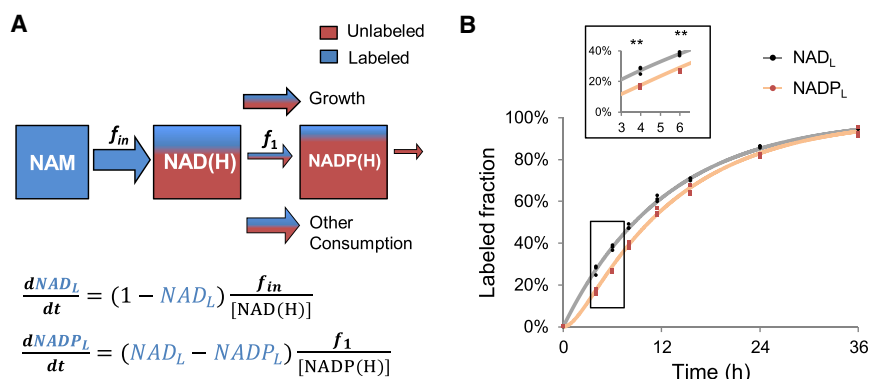
A

Legend:
- Unlabeled
- Labeled

$$\frac{dNAD_L}{dt} = (1 - NAD_L)\frac{f_{in}}{[NAD(H)]}$$

$$\frac{dNADP_L}{dt} = (NAD_L - NADP_L)\frac{f_1}{[NADP(H)]}$$

B

Figure 2. NAD Kinase Flux

(A) Approach to calculate NAD consumption by NAD kinase (f_1, forward flux).

(B) Labeling dynamics; symbols, experimental data (n = 3); lines, fit to differential equations in (A). **p < 0.01, paired t test; dots, experimental data, n = 3.

See also Figure S1.

change in NAD pool and flux determination based on data taken at early time points after PARP inhibition, the impact of such errors should be small. Thus, in T47D cells, approximately one-third of NAD consumption is due to basal PARP1/2 activity.

PARP is thought to be the major NAD consumer in cells with DNA damage (Wang et al., 2014; Rouleau et al., 2010). In the absence of DNA damage, basal PARP activity, as measured by the accumulation of protein poly-ADP-ribosylation in cell lysates with poly(ADP-ribose) glycohydrolase inhibitor added, was recently reported to vary markedly across cancer cell lines (Krukenberg et al., 2014). We compared PARP-mediated NAD flux in five human breast cancer cell lines with basal lysate PARylation activities (Krukenberg et al., 2014). We found that the two cell lines with relatively high accumulation of PARylation in lysates (KPL1 and MCF7) did not exhibit lower NAD concentration or higher PARP-mediated NAD consumption than the three cell lines with relatively low PARylation (AU565, SKBR3, and T47D) (Figure 3D; Table S2). This suggests that cellular PARP1/2 flux is determined by factors distinct from PARP activity as captured by lysate assays.

One potential explanation is that PARP activity is determined mainly by cellular factors, such as DNA damage, which may not be reliably captured in lysates. Constitutive DNA damage due to genetic defects in DNA repair has been reported to decrease NAD pools (Fang et al., 2014). We investigated cells with dysfunction in the DNA repair protein xeroderma pigmentosum group A (XPA) and a matched control line that was rescued by XPA transfection (Fang et al., 2014). Compared with XPA-restored cells, XPA-deficient cells suffer from chronic DNA damage, and exhibit lower steady-state NAD concentration (Fang et al., 2014) (confirmed in Figure S2A). We observed faster NAD labeling (Figure S2B) and an associated larger total NAD consumption flux in the XPA-deficient cells (Figure 3E). Moreover, the PARP contribution (as measured by adding olaparib together with labeled NAM) was larger. Thus, while we do not observe a relationship between basal lysate PARylation activities and NAD flux, we capture the known link between compromised DNA repair, PARP, and NAD consumption.

To investigate the effects of acute DNA damage, we treated T47D cells with zeocin to trigger DNA double-strand breaks at the same time as switching into [²H]NAM and analyzed total and ²H-NAD after 8 hr. Zeocin reduced total NAD to ~60% of control, mainly by accelerating the loss of unlabeled NAD, and this effect was blocked by olaparib (Figure 3F). Quantitative anal-

ysis revealing ~2× increase in f_{out} that was reversed by co-treatment with PARP inhibitor (Figure 3G). Thus, PARP consumes about one-third of NAD under basal conditions and becomes the dominant consumer in the presence of overt DNA damage. These observations capture the quantitative change in flux during DNA damage, although harsher damage might lead to a yet more dramatic change (Zong et al., 2004).

To evaluate contributions from other pathways, we monitored the increase in NAD pool size and labeling pattern in T47D cells treated with sirtinol (a SIRT1/2 inhibitor) and EX527 (a SIRT1 inhibitor) (Figures 3H, S2C, and S2D). We observed a significant decrease in f_{out}. Quantitatively SIRT1/2 consume about one-third of NAD under basal conditions (32 pmol per million cells per hr, CI: 24–41), similar to consumption by PARP1/2. The effect of dual PARP1/2 and SIRT1/2 inhibition was roughly additive. The flux measurements lack the precision to assess whether PARP inhibition is activating sirtuins, or vice versa, but the data do confirm that PARP1/2 and SIRT1/2 collectively account for the majority of NAD consumption (Figures 3I and 3J).

We then examined two additional cell lines, the transformed but non-tumorigenic breast cell MCF7 and differentiated C2C12 myotubes (Figures S2E–S2I). Comparison of NAD labeling with cellular growth rate revealed that most NAD in the MCF7 cells was passed along to their daughter cells, whereas in the differentiated C2C12 cells, essentially all NAD was consumed, as expected based on their post-mitotic status (Figure 3K). Similarly, among different proliferating cell lines, growth rate and NAD usage for growth were correlated (R^2 = 0.48, p = 0.01; Figure S2K). In both MCF7 cells and C2C12 myotubes, based on NAM-tracer experiments with olaparib and sirtinol, the relative contributions of PARP1/2 and SIRT1/2 were similar. Thus, across several cell lines, NAD consumption by PARP1/2 is similar to that by SIRT1/2 (Figures 3K and 3L).

Impact of NAD Concentration on Fluxes

The rate of enzymatic reactions depends on substrate concentration, so we expect an effect of concentrations on fluxes. To test whether such a relationship exists for NAD consumption, we first treated cells with FK866, an NAMPT inhibitor in clinical trials (Zerp et al., 2014), simultaneously with switching into [²H]NAM. As expected, FK866 almost completely blocked NAD labeling. We then assessed whether the resulting drop in NAD concentration altered NAD consumption kinetics. The decline in NAD concentration following addition of FK866 approximated a single-exponential decay (Figure 4A), which implies that NAD consumption depends linearly on its concentration: f_{out} = k
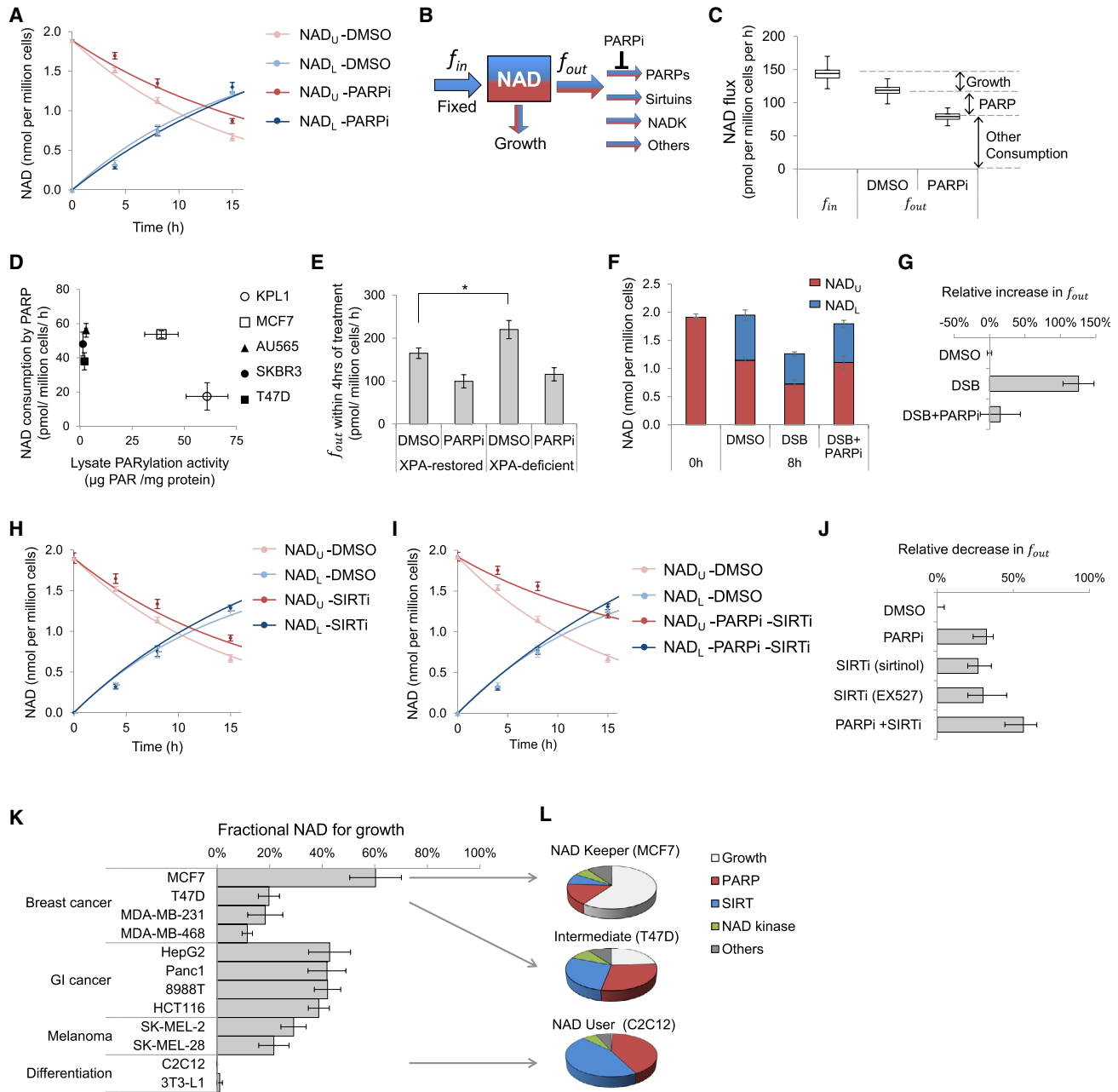
Figure 3. NAD Utilization in Cell Lines

(A) NAD concentration and labeling in T47D cells treated with olaparib (10 μM, PARP1/2 inhibitor). Olaparib was added simultaneously with switching cells into [^{2}H]NAM. Symbols, experimental data (mean ± SD, n = 3); lines, fit to equations corresponding to model in (B) (STAR Methods).

(B) Approach to calculate NAD consumption by different enzymes, based on assumption of fixed NAD production flux and decreased consumption flux upon adding inhibitor.

(C) Fitted NAD efflux based on NAD concentration, cell growth rate, and isotope labeling in the presence or absence of 10 μM olaparib, as shown in (A). Horizontal line within box, best fit; box, interquartile range; whisker, 95% confidence intervals.

(D) PARylation activity and PARP-mediated NAD consumption as measured by isotope tracing in the presence and absence of 10 μM olaparib are not correlated across five breast cell lines. Lysate and MagPlex beads were incubated together overnight to measure PARylation activity (Krukenberg et al., 2014). Data are mean ± SD, n = 3.

(E) Total NAD consumption fluxes in XPA-deficient or XPA-restored cells treated with DMSO or olaparib, calculated from [^{2}H]NAM labeling in the first 8 hr of drug treatment. Results are normalized to untransfected XPA-deficient cells; data are mean ± SD, n = 3; *p < 0.05, paired t test.

(F) NAD concentration and labeling in T47D cells incubated simultaneously with [^{2}H]NAM and zeocin (250 μg/mL, to induce DNA double-strand break), with or without olaparib, for 8 hr. Data are mean ± SD, n = 3.

(G) Increase in total NAD consumption flux based on data in (F) (mean with 95% confidence interval).
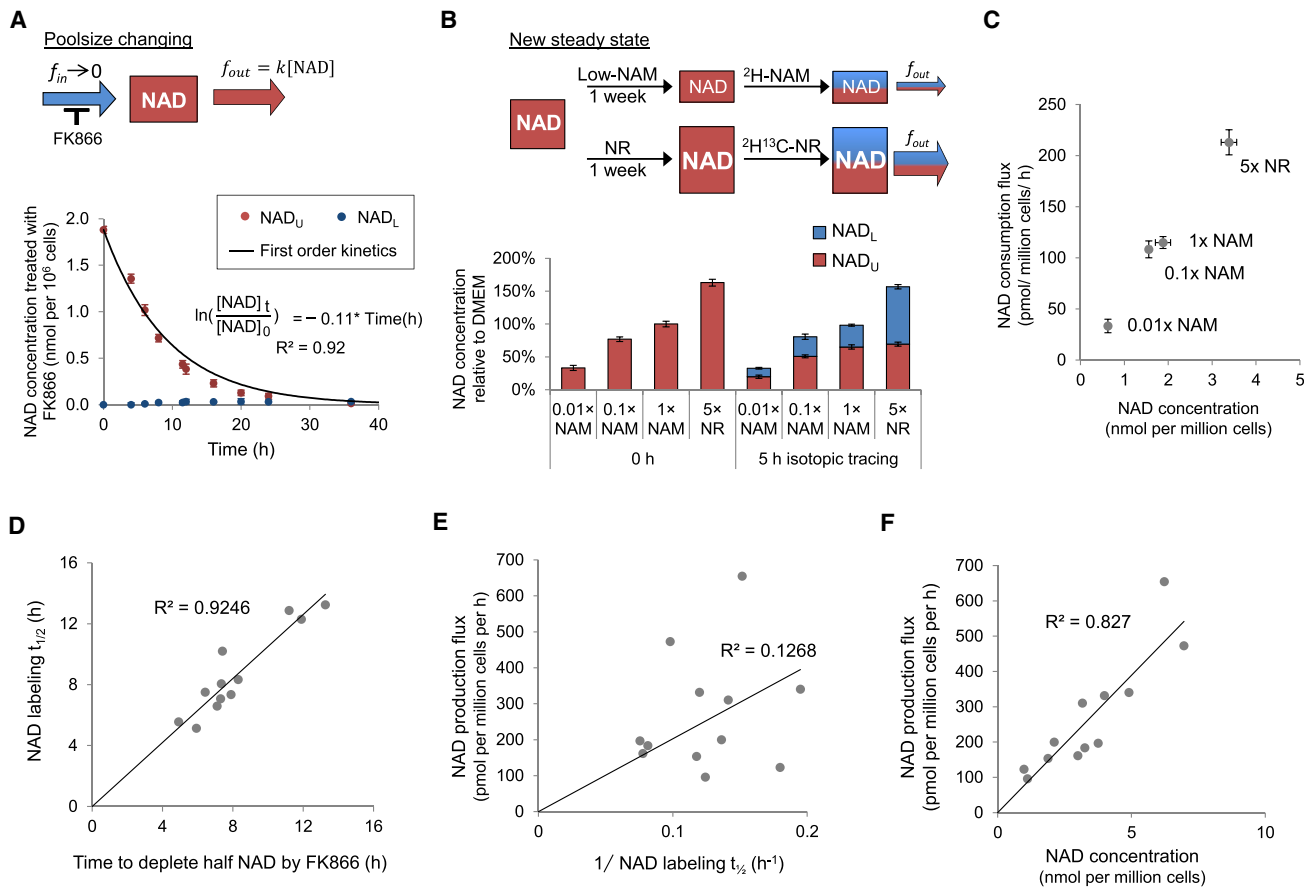
Figure 4. Relationship between NAD Concentration and Flux in Cell Lines

(A) NAD concentration and labeling in T47D cells treated with FK866 (100 nM, NAMPT inhibitor). FK866 was added simultaneously with switching cells into $[^2H]$ NAM. Symbols, experimental data (mean ± SD, n = 3); line, fit to equations corresponding to the illustrated kinetic scheme, which assumes that NAMPT fully blocks NAD synthesis and NAD consumption is proportional to its concentration ("first-order kinetics").

(B) NAD concentration before and after labeling for 5 hr. T47D cells were pre-treated with 1× NAM (standard DMEM condition), 0.1× NAM, or 0.01× NAM, for 1 week and labeled with the same concentration of $[^2H]$NAM, or were pre-treated with 5× NR for 4 days and labeled with the same concentration of $[^2H,^{13}C]$NR. Data are mean ± SD, n = 4.

(C) Correlation between NAD concentration and consumption flux based on data in (B).

(D) Correlation between $t_{1/2}$ for NAD labeling by $[^2H]$NAM and $t_{1/2}$ for NAD depletion upon adding FK866 (100 nM) across 12 cell lines. Each dot represents one cell line. For data by cell line, see Table S3.

(E) Across the same 12 cell lines, NAD flux correlates poorly with labeling $t_{1/2}$.

(F) NAD flux correlates more strongly with intracellular NAD concentration.

See also Table S3.

[NAD]. To further test the relationship between [NAD] and f_{out}, we reduced the medium NAM to 0.1× or 0.01× of its normal concentration in DMEM (i.e., to roughly 1.5× and 0.15× normal circulating levels) or added NR at 5× the normal media NAM concentration, resulting in a 20% decrease, 70% decrease, or

60% increase in [NAD], respectively (Figure 4B). We then switched to isotopic NAM or NR at the same concentration and observed that f_{out} was roughly proportional to [NAD] (Figures 4B and 4C). Because PARP1/2 and SIRT1/2 are major consumption enzymes, these data suggest that, at least in in T47D cells,

(H) NAD concentration and labeling in T47D cells treated with sirtinol (25 μM, Sirtuin 1/2 inhibitor). Sirtinol was added simultaneously with switching cells into $[^2H]$ NAM. Symbols, experimental data (n = 3); line, fit to equations.

(I) Same as (H) but with dual PARP and SIRT1/2 inhibition.

(J) Decrease in NAD consumption, calculated based on first 4 hr after drug exposure in T47D cells, for olaparib (10 μM, PARP1/2 inhibitor), sirtinol (25 μM, Sirtuin 1/2 inhibitor), EX527(10 μM, Sirtuin 1/2 inhibitor), and co-treatment of olaparib (10 μM) and sirtinol (25 μM) (mean with 95% confidence interval).

(K) Fraction of NAD directed toward supporting growth in different cell lines cell lines, as determined by experimental measurements of growth rate relative to NAD isotope labeling rate (mean with 95% confidence interval).

(L) Pie graphs indicating NAD fates in differentiated myocytes (C2C12 cells) and proliferating T47D and MCF7 cells. Consumption routes in C2C12 cells and MCF7 cells were determined as for T47D cells (see Figure S2 for data in C2C12 cells and MCF7 cells).
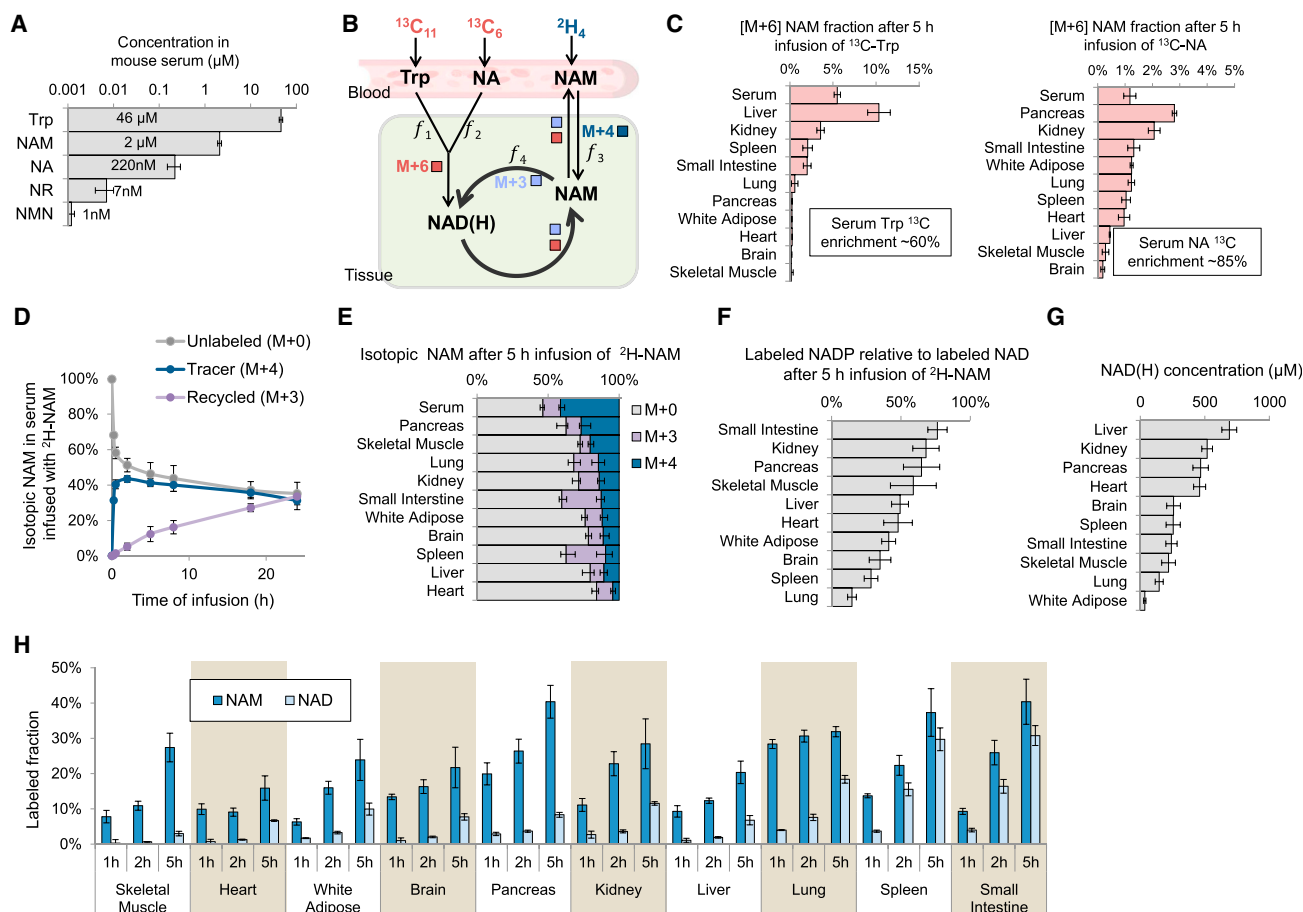
See also Figure S2 and Table S2.

Figure 5. Contributors to NAD Biosynthesis *In Vivo* in Mice

(A) Concentration of NAD contributors (log scale, mean ± SD, n = 4).

(B) Schematic of tryptophan (Trp) and NAM tracer metabolism. [^{13}C]Trp was infused via the jugular vein at 5 nmol/g/min and [^{2}H]NAM at 0.3 nmol/g/min; tryptophan to NAD flux (f_1), NA to NAD flux (f_2), NAM uptake from circulation (f_3), and NAMPT flux (f_4).

(C) Serum and tissue isotope labeling of NAM from 5 hr [U-^{13}C]Trp infusion (left), or from 5 hr [^{13}C]NA infusion (right) (mean ± SD, n = 3).

(D) Serum isotope labeling of NAM from [^{2}H]NAM infusion. Symbols, experimental data (mean ± SD, n = 3); lines are to guide the eye.

(E) NAM labeling from [^{2}H]NAM infusion.

(F) Labeled NADP(H) relative to labeled NAD(H) in tissues after 5 hr [^{2}H]NAM infusion.

(G) NAD(H) concentration across tissues.

(H) Labeled fractions of NAM, NAD, and NADPH in tissues after 1, 2, and 5 hr of [^{2}H]NAM infusion. For (E)–(H), data are mean ± SD, n = 3. For related cell culture experiments, see also Figures S3, S4, and S5 and Tables S1 and S4.

---

their cellular activities are substantially determined by NAD concentration.

To measure NAD consumption and its dependence on NAD concentration in more cell types, we measured NAD dynamics in response to FK866 across 12 cell lines (3 other breast cancer cell lines, 4 gastrointestinal cancer cell lines, 2 melanoma cell lines, and differentiated myocytes and adipocytes). Across these cell lines, the $t_{1/2}$ for NAD depletion by FK866 was nearly identical to NAD labeling $t_{1/2}$ in the absence of drug (R^2 = 0.92, slope = 1.03, p < 0.005) (Figure 4D; Table S3). Different cell lines varied in NAD demand for growth (Figure 3K), NAD concentration (from 1 to 7 nmol per million cells) and labeling half-time (5–14 hr). Together, [NAD] and labeling $t_{1/2}$ determine NAD synthesis flux (f_{in} = ln2[NAD]/labeling $t_{1/2}$). Interestingly, [NAD] was more variable than $t_{1/2}$ and thus exerted greater influence over f_{in}. Indeed,

we found a strong correlation between NAD concentration and synthesis flux (R^2 = 0.81, p < 0.005), but no correlation between $t_{1/2}$ and flux (Figures 4E and 4F). These data are consistent with high production flux leading to a large NAD pool size, with the consumption rate in cell lines proportional to [NAD]. One practical implication of this finding is that NAD flux can be estimated in tissue culture by the kinetics of NAD loss after blocking NAMPT, without the need for isotope tracer methods.

Tissue Heterogeneity in NAD Synthesis

We next employed isotope tracing to probe whole-organism NAD metabolic fluxes. In mammalian plasma, tryptophan, NAM, and NA are the only NAD precursors with concentrations >0.1 μM (Figure 5A). We accordingly selected [U-^{13}C]Trp, [2,4,5,6-^{2}H]NAM, and [U-^{13}C]NA for *in vivo* tracing studies

(Figure 5B; for their effects *in vitro*, see Figures S3 and S4). Infusions were performed on 12- to 14-week-old C57BL/6 mice precatheterized on the right jugular vein, aiming to quantify in a tissue-specific manner (1) biosynthetic flux from tryptophan and NA to NAD, (2) salvage flux from tissue NAM to NAD, (3) exchange flux between tissue NAM and serum NAM, and (4) NAD kinase flux.

Infusion of [U-^{13}C]Trp (M+11) at a consistent rate of 5 nmol per g mouse body weight per min rapidly resulted in approximately 60% serum tryptophan labeling, with accumulation over ~24 hr of serum NAM M+6 (six carbon atoms from tryptophan are retained in NAD and NAM) (Figure S5A). Tissue sampling at 5 hr revealed preferential NAM labeling in the liver. Liver NAM was labeled in excess of circulating NAM, whereas NAM in all other tissues was labeled less than circulating NAM (Figure 5C). A straightforward interpretation is that, like cell lines, most tissues do not make NAD by *de novo* synthesis, and instead rely on NAM synthesized and released from liver. Infusion of [U-^{13}C]NA (M+6) at a consistent rate of 0.02 nmol per g per min resulted in 85% serum NA labeling. This high extent of labeling, despite the low infusion rate, indicates that endogenous NA circulatory turnover flux is small, i.e., there is little flux from circulating NA into tissues, or vice versa (Hui et al., 2017). Thus, circulating NA seems to be a minor contributor to endogenous NAD production in most tissues. Consistent with this, even though the labeled NA infusion had increased the circulating NA level several-fold, the contribution of NA to serum NAM was low (1% after 5 hr, compared with 5% after 5 hr from tryptophan infusion; Figure 5C). Quantitative analysis, which takes into account the extent of circulating precursor labeling, indicates that the flux from circulating tryptophan to serum NAM exceeds the flux from NA to NAM (even after the elevation of circulating NA by the labeled infusion) by roughly an order of magnitude.

We then investigated flux from circulating NAM to tissue NAD. Infusion of [2,4,5,6-^{2}H]NAM at a consistent rate of 0.2 nmol/g/min resulted in approximately 50% serum NAM labeling, with a rapid increase in NAM M+4 and slow accumulation of NAM M+3, which is formed by assimilation of NAM M+4 into NAD, loss of the redox-active hydrogen, and subsequent cleavage of NAD to NAM (Figure 5D). Tissue NAM was less labeled than serum NAM, with the extent of labeled NAM assimilation variable across organs (Figure 5E). Thus, in contrast to cell lines where NAM exchange with the medium is fast, *in vivo*, exchange between the blood stream and tissues is slow and thus potentially an important site of regulation.

The extent of recycling of assimilated NAM M+4 into NAM M+3 varied by organ, being greatest in the spleen and small intestine and least in the skeletal muscle, suggesting rapid NAD turnover in the spleen and small intestine and slow turnover in the muscle (Figure 5E). Next, we measured NAM, NAD, and NADPH tissue labeling at multiple time points (for tissue-specific NAM, NAD, and NADPH concentrations, see Table S4). NADP(H) labeled detectably more slowly than NAD(H), and the relative labeling (Figure 5F) allowed us to calculate NAD kinase forward flux and NADP(H) turnover. Particularly slow NADPH labeling was observed in the lung. As in cell culture, the NAD kinase forward flux is a modest NAD consumer, accounting for ~25% of total net cellular NAD production

(the sum of f_1 +f_2 +f_3 in Figure 5B). The skeletal muscle showed the greatest lag between NAM and NAD labeling, and the slowest NAD labeling overall, confirming slow NAD turnover, whereas the spleen and small intestine showed the fastest NAD labeling (Figure 5H).

To gain a more complete picture of tissue-specific NAD metabolism, we used the NAM-, tryptophan-, and NA-tracing data to quantitate NAD fluxes in each tissue (f_1, f_2, f_3, f_4 in Figure 5B; Table S5). The flux model assumes both spatial homogeneity (i.e., each tissue as a single well-mixed pool) and metabolic (but not isotopic) steady state. NAM is eliminated from cells by excretion of it or one of its metabolic products such as N-methylnicotinamide (Figure S5). For half of the tissues, the model was able to fit the experimental data well, i.e., without significant systematic error; for the other half of the tissues, some systematic misfit was observed (Figure S6; Table S5). The misfitting mainly reflected a discrepancy in NAM labeling rate over time, e.g., in the lung, NAM labeling at 1 hr was too great relative to 5 hr to be accounted for given the assumption that the tissue is a single well-mixed pool. Thus, in half of tissues, we obtained evidence for compartmentation, either between cells within the tissue or within the individual cells. Alternatively, it is possible that another unmodeled factor impacted the labeling. Despite these complications, the resulting optimized flux set (Figure 6A; Table S5) accurately accounted for labeling patterns after co-infusion of [U-^{13}C]Trp and [2,4,5,6-^{2}H]NAM (20:1 ratio, equal to their physiological ratio in serum) and co-infusion of [U-^{13}C]NA and [2,4,5,6-^{2}H]NAM (1:10 ratio, equal to their ratio in serum) (Tables S6 and S7).

This quantitative analysis confirmed that the liver is the main producer of circulating NAM from tryptophan, with the kidney also net excreting NAM made from both tryptophan and NA (Figure 6A). Tissue fluxes are reported in units of molarity per time, i.e., are normalized to tissue volumes. Correcting for the larger volume of the liver relative to the kidney, the fraction of total NAM production by the liver is >95%. The other examined tissues differed dramatically in their rates of NAD turnover, with the small intestine and spleen having a flux more than 40-fold greater than muscle or fat (Figures 6A and 6B). There was a trend toward higher expression of NAD-consuming enzymes in the tissues with faster NAD turnover flux, but no strong correlation with any particular NAD-consuming enzyme (Figure 6B). In contrast to cell lines, where flux through NAD correlated more strongly with NAD concentration than turnover half-time, *in vivo* the reverse was true (Figures 6C and 6D). This indicates large tissue-specific differences in NAD consumption pathway activities. Notably, while standard tissue culture cell lines showed similar NAD turnover half-times irrespective of their tissue of origin, half-times varied by 50-fold across tissues *in vivo*, with the half-time for NAD turnover in the small intestine more than 10-fold faster than in any tested cultured cell line (Figure 6E). Based on the striking differences between cultured cell lines and tissues *in vivo*, we examined fluxes in freshly isolated primary hepatocytes. Like liver, and in contrast to HepG2 cells, the freshly isolated hepatocytes produced NAD from tryptophan and manifested a fast NAD turnover time of ~2 hr (Figure 6F). Thus, mammalian NAD metabolism involves extensive tissue-specific pathway regulation, which is not replicated in standard cell lines.
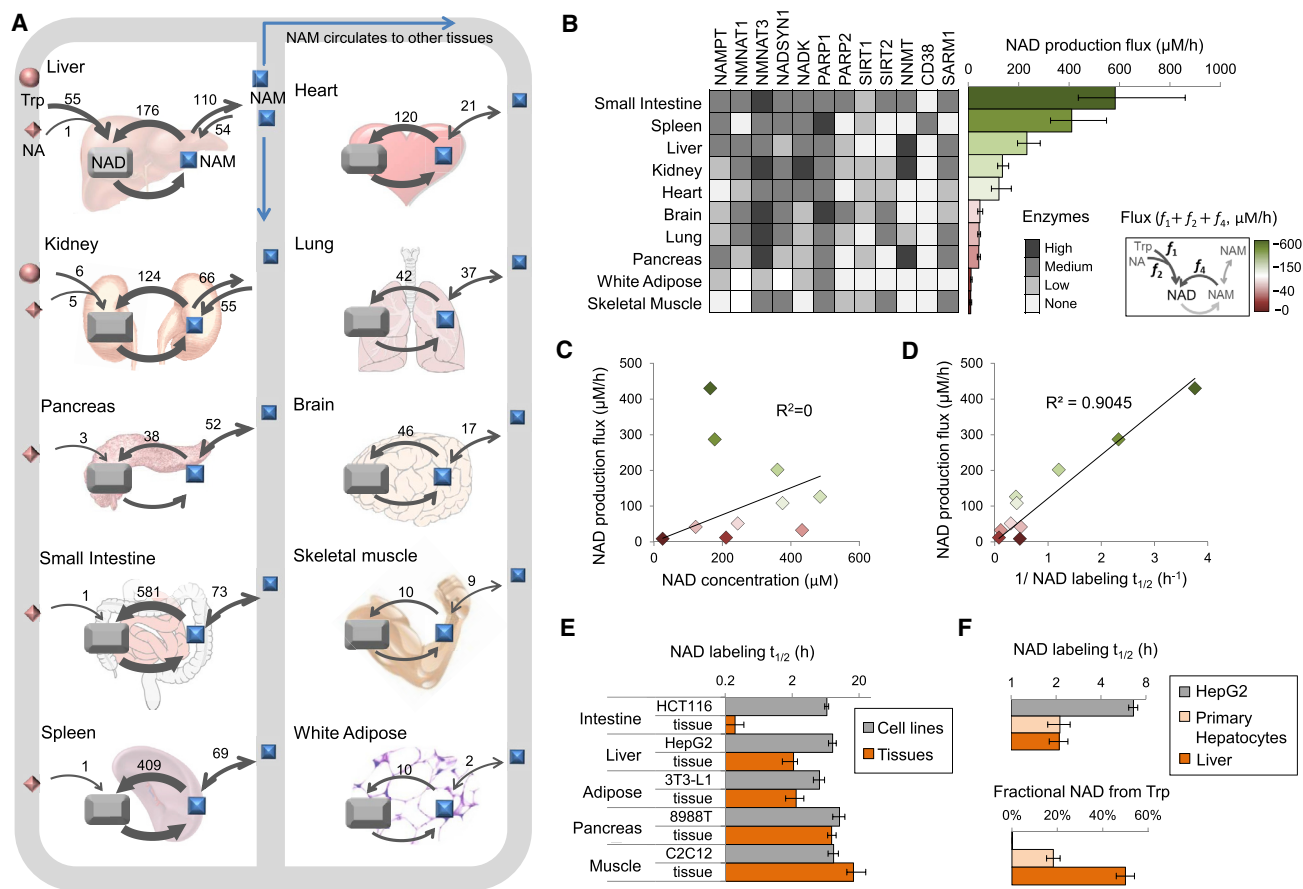
Figure 6. NAD Turnover in Tissues

(A) Quantitative NAD fluxes in tissues, based on metabolic flux analysis informed by liquid chromatography-mass spectrometry measurement of metabolite labeling in serum and tissues after separate infusions of [^{13}C]Trp, [^{13}C]NA, and [^{2}H]NAM. Values shown are fluxes (μM/hr) from the best fit flux sets for network in (B). For complete flux sets, see Table S5. Fluxes shown for tryptophan and NA reflect net assimilation into NAD. For NAM, there is significant net export from the liver and kidney. For these two tissues, we show separately the uptake and excretion fluxes of NAM, as determined by modeling of the tissue-labeling data. For all other tissues, NAM uptake and excretion are balanced, and we show only a single value corresponding to the exchange rate between the tissue and circulation.

(B) Total NAD production flux ($f_1 + f_2 + f_4$) across tissues and relevant NAD enzyme protein expression levels based on antibody staining from http://www.proteinatlas.org/.

(C and D) Across tissues, NAD production flux (B) correlates with inverse labeling half-time, but not NAD concentration.

(E) NAD labeling half-time across cell lines and corresponding mouse tissues.

(F) NAD labeling half-time and Trp fractional contribution in HepG2 cells, primary hepatocytes, and *in vivo* liver.

Bars are mean with 95% confidence intervals.

See also Figure S6 and Tables S5–S7.

Tracing the Fate of NR and NMN

While tryptophan, NA, and NAM are the physiological circulating NAD precursors, NR and NMN have garnered much attention as potential alternative precursors for use as nutraceuticals to elevate NAD. These precursors can be incorporated into NAD without breaking the nicotinamide-ribose linkage, allowing them to bypass the gating NAMPT reaction, which is subject to feedback inhibition by NAD (Ratajczak et al., 2016; Frederick et al., 2016). NR and NMN boost NAD levels *in vitro* and *in vivo*, and have shown promise in a number of rodent disease models (Revollo et al., 2007; Cantó et al., 2012; Yang and Sauve, 2016). To probe their metabolism, we employed versions of NR and NMN that are isotopically labeled on both the nicotinamide and ribose moieties. This allowed us

to distinguish NAD made directly from NR or NMN (M+2) versus NAD made from NAM-derived NR or NMN (M+1) (Figure 7A). While reasonably stable in tissue culture medium ($t_{1/2} \sim 12$ hr) (Figure S4G), both NR and NMN were quickly degraded to NAM in whole blood ($t_{1/2}$ 3 min) (Figures 7B, 7C, and S4H). Accordingly, we flash-froze blood specimens and then later extracted them with −80°C methanol (80:20). NR and NMN were administered by i.v. bolus or oral gavage at 50 mg/kg, which is equivalent to 290 mg in a 70-kg human on a body surface area basis, in the range of common nutraceuticals. The limits of detection for measurement of NR and NMN were 0.1 and 0.2 nM, respectively. Readily detectable concentrations of intact NR were observed in the blood following i.v., but not after oral, administration, indicating nearly complete first-pass
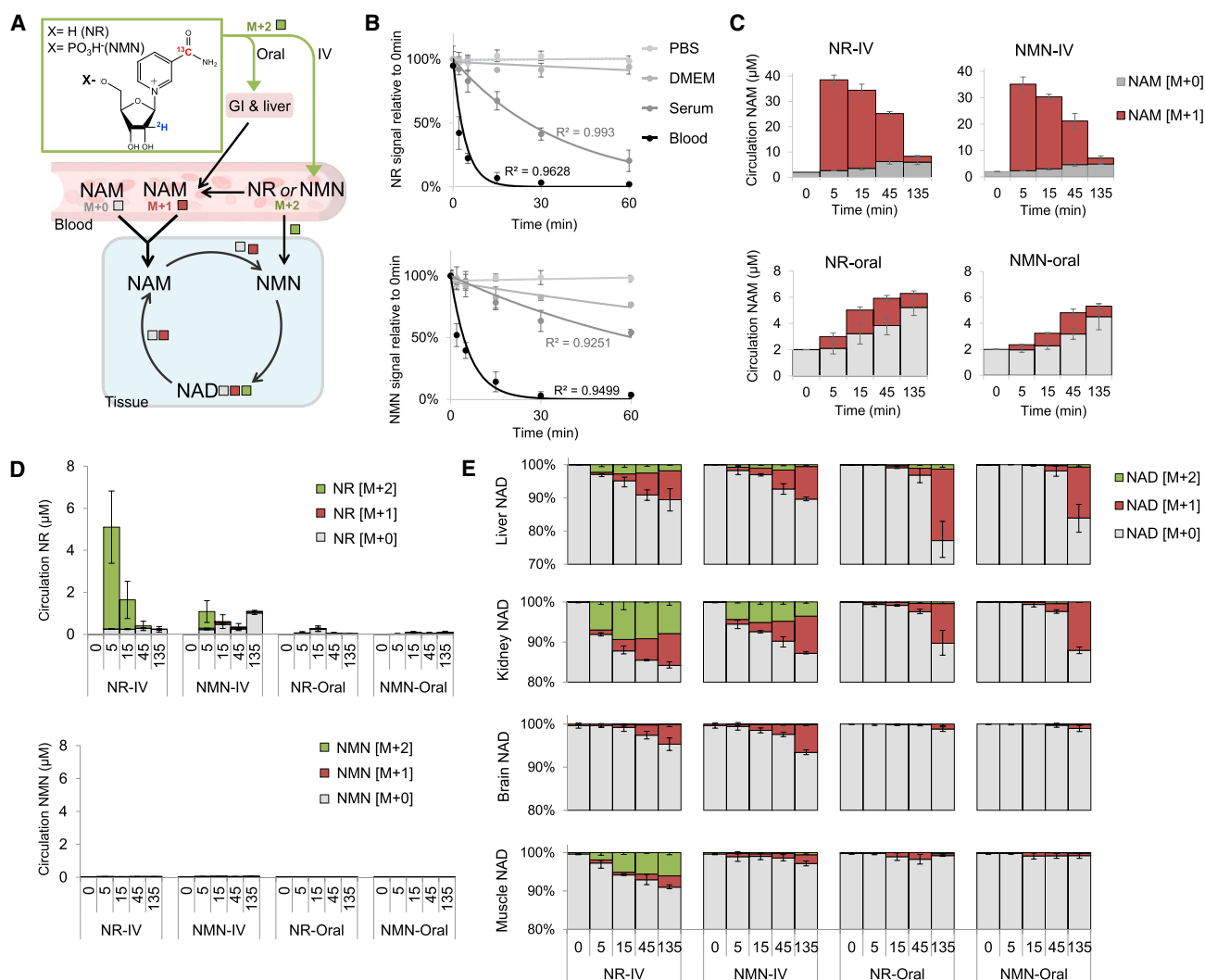
Figure 7. NR and NMN Are Effectively Delivered to Tissues by i.v., but Not Oral, Administration

(A) Schematic of [^{2}H,^{13}C]NR and [^{2}H,^{13}C]NMN metabolism *in vivo*. NAD made directly from NR or NMN is M+2 labeled. NAD made from NAM-derived NR or NMN is M+1 labeled. Previously made NAD, or NAD made from unlabeled NAM, is unlabeled (M+0).

(B) Stability of NR and NMN standards in PBS, DMEM with 10% DFBS, mouse serum, or mouse blood. Symbols, experimental data (mean ± SD, n = 3); lines, single-exponential fits.

(C) Circulating NAM from tail bleeds at the indicated times after a 50-mg/kg bolus of [^{2}H,^{13}C]NR or [^{2}H,^{13}C]NMN by oral gavage or by i.v. injection.

(D) Corresponding circulating NR and NMN.

(E) Corresponding tissue NAD labeling.

Data are mean ± SD, n = 3.

See also Figures S4 and S7.

metabolism (Figures 7D and S7). NMN was barely detectable even after i.v. administration; its i.v. dosing did, however, result in a rise in circulating NR. Irrespective of the route of delivery, the main circulating product of the administered NR or NMN was NAM, which increased by ~20× within 5 min of i.v. NR or NMN; oral NR or NMN administration led to a more modest rise in circulating NAM (Figure 7C).

Examination of tissue NAD labeling indicated some direct assimilation of oral NR and NMN into liver NAD, based on M+2 labeling, which made up a minority of the signal, but was nonetheless readily detectable. The active formation of liver NAD from

NR and NMN is consistent with both compounds being subject to substantial hepatic first-pass metabolism. In contrast, extra-hepatic tissues displayed minimal M+2 NAD (Figure 7E), suggesting that orally delivered NR and NMN are converted into NAM before reaching the systemic circulation. Intravenous injection of NR or NMN, on the other hand, resulted in substantial M+2 NAD in both the liver and kidney. To explore whether higher oral doses of NR were also cleared by the liver, we examined the dynamics of tissue NAD labeling from 200 mg/kg i.v. or oral doubly labeled NR. Similar to the 50 mg/kg dose, the 200 mg/kg dose resulted in M+2 NAD in the liver but not the muscle or kidney after

oral administration (Figure S7A). Thus, even very high doses of oral NR do not reach tissues intact.

In the brain, we detected only M+1 NAD, indicating a reliance on circulating NAM and suggesting that intact NR and NMN may not cross the blood-brain barrier (Figure 7E). This was also true after i.v. administration of a very high dose of NR or NMN (500 mg/kg; Figure S7B). Interestingly, NR but not NMN was efficiently assimilated intact into NAD in the muscle (Figure 7E). This preference of muscle for NR held true also at 500 mg/kg i.v. (Figure S7B). To our knowledge, this is the first clear example of a differential metabolic effect between these two compounds *in vivo*. Tissue-specific utilization of different precursors should be considered in the design of future NAD-boosting drugs.

DISCUSSION

NAD plays a central role in epigenetics and energy metabolism. It is accordingly important to measure NAD production and consumption pathways, and how they differ across cell types, tissues, physiological states, and diseases. In addition, it is important to understand the impact of drugs and nutraceuticals on NAD metabolism. Here we present an isotopic-tracing approach to quantify NAD synthesis and consumption fluxes: introduction of labeled NAM or other NAD precursors followed by measurement of NAD labeling. Both NAM and NAD are sufficiently abundant and stable for facile measurement of their quantitative labeling by liquid chromatography-mass spectrometry, rendering the methods well suited for broad application.

In steadily growing cell lines, NAD labeling follows single-exponential kinetics (Figure 1B). The disappearance rate of unlabeled NAD in the presence of labeled NAM reflects the total activity of all consumption pathways. By tracing label incorporation into NADP(H) we showed that NAD kinase accounts for 10% of NAD consumption (Figure 2). By combining this isotope tracer measurement with pharmacological modulation of PARP1/2 and SIRT1/2, we were able to assign each enzyme class a substantial (∼1/3) role in NAD consumption under basal conditions (Figure 3J). As expected, cells defective in DNA repair or suffering acute DNA damage had faster PARP-mediated NAD consumption, which validated our method and quantified the effect of DNA damage on flux through the PARPs. In contrast, neither PARP expression levels nor activity in lysate was predictive of the basal PARP-mediated NAD consumption flux in cell lines. We did not observe substantial NAD consumption by CD38 in cell culture (based on inhibition with quercetin and apigenin; Figure S2H), although genetic evidence suggests that CD38 plays a substantial role in NAD consumption *in vivo* (Sahar et al., 2011; Chiang et al., 2015).

Typical cell culture medium contains only two potential NAD precursors, NAM and tryptophan (National Research Council, 1989). In our hands, primary hepatocytes were the only cell type capable of using tryptophan for NAD synthesis, indicating that the vast majority of cells depend entirely on NAM. In animals, gene data indicate expression of the enzymes required for *de novo* synthesis of NAD from tryptophan in the liver and kidney (Figure S5D), and the concentration of tryptophan in the diet has been reported to affect the liver NAD levels (Powanda and Wannemacher, 1970). Consistent with this, quantitative analysis of *in vivo* tracing data with labeled NAM and tryptophan indicated

de novo NAD synthesis from tryptophan in the kidney and, to a much greater extent, the liver. Other tissues, in contrast, relied almost exclusively on circulating NAM made by the liver. Liver synthesis of NAD and excretion of NAM occurred even when serum NAM was elevated by co-infusion of tryptophan and NAM; thus, liver constitutively produces NAM to support NAD synthesis throughout the rest of the body (Figure 6A).

To explore the relationship between NAD concentration and fluxes, we changed medium levels of NAM and NR, as well as added FK866, thereby manipulating the intracellular NAD concentration in cultured cells across an ∼10-fold range. NAD consumption flux correlated strongly with NAD concentration; this correlation results in NAD turnover time being relatively consistent (∼8 hr, substantially longer than the 1–2 hr half-life previously estimated for DH98/AH2 cells, which were not included in the present study; Hillyard et al., 1973; Rechsteiner et al., 1976b). The simplest explanation for the correlation between NAD concentration and flux is that consumption flux is a linear function of the concentration of NAD, the enzymes' substrate. According to Michaelis-Menten kinetics, such a linear relationship is expected only when substrate is subsaturating. We observed an average whole-cell concentration of NAD ranging from 0.1 to 2 mM, with the T47D cells in which we conducted the nutrient perturbation experiments having 0.6 mM. While this is similar to or below the K_m of NAD kinase (0.6–1 mM) (Ohashi et al., 2012), it exceeds the reported NAD K_m of PARP1 (0.1–0.2 mM) (Gibson et al., 2016; Langelier et al., 2010; Beneke et al., 2000) and most of the (quite variable) literature estimates of sirtuin K_m values (0.01–0.6 mM). While these biochemical data suggest that PARPs and sirtuins should be substantially saturated at 0.6 mM NAD, physiological K_m values are often higher than those measured in a test tube, due to active site competition from other metabolites in the cellular milieu (Yuan et al., 2009). In addition, NAD and NADH are often protein bound, and the free NAD concentrations within cytosol and/or mitochondria may be considerably less than the whole-cell averages or the K_m values for consuming enzymes (Nikiforov et al., 2011). Thus, the simplest biochemical explanation for the correlation between NAD concentrations and fluxes is a roughly linear dependence of PARP and sirtuin activity on NAD concentration.

In contrast to the relatively consistent NAD turnover half-time in cell culture of 6–12 hr, NAD turnover rates varied dramatically across tissues (Figure 6E). In several tissues, NAD turnover was substantially faster than in any of the cultured cell lines that we examined. On the flip side, in the skeletal muscle, it was substantially slower. This variation in NAD turnover rate between tissues *in vivo* highlights the importance of understanding the mechanisms controlling NAD fluxes. Across tissues, we did not observe a strong correlation between flux and NAD concentration or the protein levels of known NAD consumers or biosynthetic enzymes (Figures 6B and 6C) (Mori et al., 2014). This may reflect regulation of these enzymes by other means, such as partner proteins or subcellular localization, or that other major NAD consumption pathways may remain to be discovered. For example, one open question is CD38 orientation and regulation. CD38 is thought to be a major sink for NAD in tissues, especially in older mice, as inferred from the effects of genetic ablation on NAD levels (Chiang et al., 2015; Camacho-Pereira et al., 2016).

However, in its standard ectoenzyme orientation, where the active site is not exposed to the cytoplasm, CD38 may not be active. Under some conditions, or in some tissues, it may be expressed in an inverted orientation or on an intracellular membrane, making it much more active (Zhao et al., 2015). This kind of topological regulation would not be captured in gene expression or lysate biochemical data. Clearly, much remains to be learned concerning NAD metabolism in tissues, distinct from tissue culture. We note, for example, that the hepatocellular carcinoma cell line HepG2 exhibits no NAD production from tryptophan and much slower NAD flux than mouse liver or isolated hepatocytes. This kind of differential would be masked if only steady-state NAD concentration were measured, emphasizing the importance of flux assays.

We also explored the metabolism of two NAD precursors that have recently received attention for their ability to elevate tissue NAD levels, NR and NMN. Interestingly, we found that neither compound was able to enter the circulation intact in substantial quantities when delivered orally. While the dose that we used (50 mg/kg) was modest in order to avoid severe metabolic perturbation, our result is consistent with our previous finding that 200 mg/kg oral NR contributes directly to NAD synthesis in the liver, but not the skeletal muscle (Frederick et al., 2016). Similarly, in the present experiment, lack of direct tissue assimilation of orally administered NR or NMN is evident in the labeling pattern of tissue NAD. Direct assimilation of M+2 NR or NMN would yield M+2 NAD. Turnover of M+2 NAD within a tissue could in principle produce M+1 NAD after direct NR or NMN assimilation, but our independent measurements of tissue NAD turnover (Figure 5) revealed that these fluxes are too slow to account for the lack of M+2 tissue NAD. Another hypothetical possibility is base exchange (Sauve et al., 1998; Sauve and Schramm, 2003). Without formally ruling out such a possibility, we observed that i.v. administration of either compound results in its detection within the circulation (albeit to a much greater extent for NR) and a robust M+2 peak in the kidney, proving that the route of delivery has a profound effect on the ability of these precursors to reach target tissues. Surprisingly, i.v. NR was much more effective than NMN for labeling the NAD pool in the skeletal muscle. This is consistent with the proposal that at least some tissues are incapable of taking up NMN directly (Ratajczak et al., 2016; Nikiforov et al., 2011). On the other hand, direct transport of NMN would allow its utilization even in tissues that lack NRK or NAMPT activity. Thus, it will be extremely important to consider tissue-specific enzyme and transporter expression when using NAD precursors therapeutically.

Overall, by developing broadly applicable NAD-tracing methods, we have been able to gather a substantial body of foundational data regarding NAD metabolism and its potential modulation with nutraceuticals. In some cases, such as liver being the main site of NAD de novo synthesis, we are able to validate hypotheses based on expression data. In other cases, such as NAD consumption by PARP in culture, we find that biochemical data do not predict metabolic fluxes. Perhaps most importantly, we identify many distinguishing features of the in vivo context. These include high variability in NAD turnover across tissues and nearly complete first-pass metabolism of oral NR and NMN, which likely result in these compounds having systemic effects similar to or indistinguishable from oral NAM. We also iden-tify tissue-specific preferences in NAD precursor uptake, with the muscle highly responsive to NR, but not NMN or NAM. Use of isotope tracing to understanding these fundamental features of in vivo NAD metabolism will open the door to more selective and effective interventions against aging and disease.

Study Limitations

The present study examined the production and consumption fluxes of NAD in cell culture, as well as the production of NAD in different tissues in intact mice. Although we can infer NAD turnover in vivo based on its labeling kinetics from isotopic NAM, we did not dissect the consuming enzymes involved. In addition, we did not quantify the terminal excretion of the NAM ring from the body. Establishing mass balance for whole-body nicotinamide production and consumption is an important future objective.

We also acknowledge that our in vitro dissection of NAD-consuming enzymes relied on small-molecule inhibitors, which typically suffer from both off-target effects and incomplete target inhibition. To block PARP, we employed olaparib, which is an FDA-approved drug. For sirtuins, we employed sirtinol (Wang et al., 2012; Zhou et al., 2016) and EX527, which are tool compounds. Sirtinol is known to have off-target activity (Wang et al., 2013). While we observed similar effects of sirtinol and EX527 on NAD turnover, which were consistent with sirtuin inhibition, our data do not rule out off-target effects that may be impacting our results or that could lead to erroneous conclusions in longer-term studies evaluating more distal endpoints than simply NAD turnover.

In addition, we were unable to establish a major contribution of CD38 to NAD turnover in the cell lines that were studied, despite compelling genetic evidence of its importance in vivo (Sahar et al., 2011; Chiang et al., 2015). In future studies it will be important to determine the contribution of CD38 using cells lines with more robust activity for this enzyme, or through in vivo experiments with genetic or pharmacological inhibition. In general, combining the isotope-tracing methods described here with tissue-specific knockouts of different NAD enzymes should prove a powerful approach.

STAR★METHODS

Detailed methods are provided in the online version of this paper and include the following:

- KEY RESOURCES TABLE
- CONTACT FOR REAGENT AND RESOURCE SHARING
- EXPERIMENTAL MODEL AND SUBJECT DETAILS
  - Mice
  - Cell Culture
- METHOD DETAILS
  - siRNAs, Antibodies, and Drugs
  - Isotope Labeling
  - Intravenous Infusion of Wild Type C57BL/6 Mice
  - Metabolite Measurements in Cell Lines
  - Metabolite Measurements of Serum and Tissues
- QUANTIFICATION AND STATISTICAL ANALYSIS
  - Quantification of NAD Synthesis Fluxes in Cell Lines
  - Quantification of NAD Consumption Fluxes in Cell Lines

- ○ Quantification of NAD Fluxes *In Vivo*
- ○ Statistical Analysis
- ● DATA AND SOFTWARE AVAILABILITY

AUTHOR CONTRIBUTIONS

T.J.M. and L.L. conceived the project. J.D.R., J.A.B., E.W., and X.S. conceived specific experiments. L.L. performed and analyzed most experiments. L.L., X.S., and J.D.R. conducted the flux analysis. L.L., S.H., W.J.Q., L.Z., D.W.F., and K.C. performed the *in vivo* experiments. P.R. and M.M. conducted the synthesis of isotopic NR. K.K. performed PARylation experiments. J.D.R., T.J.M., and L.L. wrote the manuscript with input from all authors.

REFERENCES

Antoniewicz, M.R., Kelleher, J.K., and Stephanopoulos, G. (2006). Determination of confidence intervals of metabolic fluxes estimated from stable isotope measurements. Metab. Eng. *8*, 324–337.

Beneke, S., Alvarez-Gonzalez, R., and Bürkle, A. (2000). Comparative characterisation of poly(ADP-ribose) polymerase-1 from two mammalian species with different life span. Exp. Gerontol. *35*, 989–1002.

Bogan, K.L., and Brenner, C. (2008). Nicotinic acid, nicotinamide, and nicotinamide riboside: a molecular evaluation of NAD+ precursor vitamins in human nutrition. Annu. Rev. Nutr. *28*, 115–130.

Bonkowski, M.S., and Sinclair, D.A. (2016). Slowing ageing by design: the rise of NAD+ and sirtuin-activating compounds. Nat. Rev. Mol. Cell Biol. *17*, 679–690.

Buncel, E., and Lee, C. (1976). Isotopes in Hydrogen Transfer Processes (Elsevier).

Camacho-Pereira, J., Tarragó, M.G., Chini, C.C.S., Nin, V., Escande, C., Warner, G.M., Puranik, A.S., Schoon, R.A., Reid, J.M., Galina, A., and Chini, E.N. (2016). CD38 dictates age-related NAD decline and mitochondrial dysfunction through an SIRT3-dependent mechanism. Cell Metab. *23*, 1127–1139.

Cantó, C., Houtkooper, R.H., Pirinen, E., Youn, D.Y., Oosterveer, M.H., Cen, Y., Fernandez-Marcos, P.J., Yamamoto, H., Andreux, P.A., Cettour-Rose, P., et al. (2012). The NAD+ precursor nicotinamide riboside enhances oxidative metabolism and protects against high-fat diet induced obesity. Cell Metab. *15*, 838–847.

Chiang, S.H., Harrington, W.W., Luo, G., Milliken, N.O., Ulrich, J.C., Chen, J., Rajpal, D.K., Qian, Y., Carpenter, T., Murray, R., et al. (2015). Genetic ablation of CD38 protects against Western diet-induced exercise intolerance and metabolic inflexibility. PLoS One *10*, e0134927.

Chini, E.N. (2009). CD38 as a regulator of cellular NAD: a novel potential pharmacological target for metabolic conditions. Curr. Pharm. Des. *15*, 57–63.

Chini, C.C.S., Guerrico, A.M., Nin, V., Camacho-Pereira, J., Escande, C., Barbosa, M.T., and Chini, E.N. (2014). Targeting of NAD metabolism in pancreatic cancer cells: potential novel therapy for pancreatic tumors. Clin. Cancer Res *20*, 120–130.

Chini, C., Tarrago, M., and Chini, E. (2017). NAD and the aging process: role in life, death and everything in between. Mol. Cell Endocrinol. *455*, 62–74.

Davar, D., Beumer, J.H., Hamieh, L., and Tawbi, H. (2012). Role of PARP inhibitors in cancer biology and therapy. Curr. Med. Chem. *19*, 3907–3921.

Fang, E.F., Scheibye-Knudsen, M., Brace, L.E., Kassahun, H., SenGupta, T., Nilsen, H., Mitchell, J.R., Croteau, D.L., and Bohr, V.A. (2014). Defective mitophagy in XPA via PARP-1 hyperactivation and NAD+/SIRT1 reduction. Cell *157*, 882–896.

Fang, E.F., Scheibye-Knudsen, M., Chua, K.F., Mattson, M.P., Croteau, D.L., and Bohr, V.A. (2016). Nuclear DNA damage signalling to mitochondria in ageing. Nat. Rev. Mol. Cell Biol. *17*, 308–321.

Fouquerel, E., Goellner, E.M., Yu, Z., Gagné, J.P., Barbi de Moura, M., Feinstein, T., Wheeler, D., Redpath, P., Li, J., Romero, G., et al. (2014). ARTD1/PARP1 negatively regulates glycolysis by inhibiting hexokinase 1 independent of NAD+ depletion. Cell Rep. *8*, 1819–1831.

Frederick, D.W., Loro, E., Liu, L., Davila, A., Jr., Chellappa, K., Silverman, I.M., Quinn, W.J., 3rd, Gosai, S.J., Tichy, E.D., Davis, J.G., et al. (2016). Loss of NAD homeostasis leads to progressive and reversible degeneration of skeletal muscle. Cell Metab. *24*, 269–282.

Gibson, B.A., Zhang, Y., Jiang, H., Hussey, K.M., Shrimp, J.H., Lin, H., Schwede, F., Yu, Y., and Kraus, W.L. (2016). Chemical genetic discovery of PARP targets reveals a role for PARP-1 in transcription elongation. Science *353*, 45–50.

Haigis, M.C., and Sinclair, D.A. (2010). Mammalian sirtuins: biological insights and disease relevance. Annu. Rev. Pathol. *5*, 253–295.

Hasmann, M., and Schemainda, I. (2003). FK866, a highly specific noncompetitive inhibitor of nicotinamide phosphoribosyltransferase, represents a novel mechanism for induction of tumor cell apoptosis. Cancer Res. *63*, 7436–7442.

Hassa, P.O., Haenni, S.S., Elser, M., and Hottiger, M.O. (2006). Nuclear ADP-ribosylation reactions in mammalian cells: where are we today and where are we going? Microbiol. Mol. Biol. Rev. *70*, 789–829.

Hayaishi, O., Ijichi, H., and Ichiyama, A. (1967). Studies on the biosynthesis of NAD by a direct method of tracing metabolism in vivo. Adv. Enzyme Regul. *5*, 9–22.

He, L., Meng, S., Germain-Lee, E.L., Radovick, S., and Wondisford, F.E. (2014). Potential biomarker of metformin action. J. Endocrinol. *221*, 363–369.

Hillyard, D., Rechsteiner, M., and Olivera, B. (1973). Pyridine nucleotide metabolism in mammalian cells in culture. J. Cell Physiol. *82*, 165–179.

Hui, S., Ghergurovich, J.M., Morscher, R.J., Jang, C., Teng, X., Lu, W., Esparza, L.A., Reya, T., Le Zhan, Yanxiang Guo, J., et al. (2017). Glucose feeds the TCA cycle via circulating lactate. Nature *551*, 115–118.

Ijichi, H., Ichiyama, A., and Hayaishi, O. (1966). Studies on the biosynthesis of nicotinamide adenine dinucleotide. 3. Comparative in vivo studies on nicotinic acid, nicotinamide, and quinolinic acid as precursors of nicotinamide adenine dinucleotide. J. Biol. Chem. *241*, 3701–3707.

Krukenberg, K.A., Jiang, R., Steen, J.A., and Mitchison, T.J. (2014). Basal activity of a PARP1-NuA4 complex varies dramatically across cancer cell lines. Cell Rep *8*, 1808–1818.

Langelier, M.F., Ruhl, D.D., Planck, J.L., Kraus, W.L., and Pascal, J.M. (2010). The Zn3 domain of human poly(ADP-ribose) polymerase-1 (PARP-1) functions in both DNA-dependent poly(ADP-ribose) synthesis activity and chromatin compaction. J. Biol. Chem. *285*, 18877–18887.

Liu, L., Shah, S., Fan, J., Park, J.O., Wellen, K.E., and Rabinowitz, J.D. (2016). Malic enzyme tracers reveal hypoxia-induced switch in adipocyte NADPH pathway usage. Nat. Chem. Biol. *12*, 345–352.

Malavasi, F., Deaglio, S., Funaro, A., Ferrero, E., Horenstein, A.L., Ortolan, E., Vaisitti, T., and Aydin, S. (2008). Evolution and function of the ADP ribosyl cyclase/CD38 gene family in physiology and pathology. Physiol. Rev. *88*, 841–886.

Menear, K.A., Adcock, C., Boulter, R., Cockcroft, X.L., Copsey, L., Cranston, A., Dillon, K.J., Drzewiecki, J., Garman, S., Gomez, S., et al. (2008). 4-[3-(4-cyclopropanecarbonylpiperazine-1-carbonyl)-4-fluorobenzyl] -2H-phthalazin-1-one: a novel bioavailable inhibitor of poly(ADP-ribose) polymerase-1. J. Med. Chem. *51*, 6581–6591.

Mori, V., Amici, A., Mazzola, F., Di Stefano, M., Conforti, L., Magni, G., Ruggieri, S., Raffaelli, N., and Orsomando, G. (2014). Metabolic profiling of alternative NAD biosynthetic routes in mouse tissues. PLoS One *9*, 1–27.

National Research Council. (1989). Recommended Dietary Allowances, Tenth Edition (National Academy Press).

Nikiforov, A., Dolle, C., Niere, M., and Ziegler, M. (2011). Pathways and subcellular compartmentation of NAD biosynthesis in human cells from entry of extracellular precursors to mitochondrial NAD generation. J. Biol. Chem. *286*, 21767–21778.

Ohashi, K., Kawai, S., and Murata, K. (2012). Identification and characterization of a human mitochondrial NAD kinase. Nat. Commun. *3*, 1248–1249.

Pirinen, E., Canto, C., Jo, Y.S., Morato, L., Zhang, H., Menzies, K.J., Williams, E.G., Mouchiroud, L., Moullan, N., Hagberg, C., et al. (2014). Pharmacological Inhibition of poly(ADP-ribose) polymerases improves fitness and mitochondrial function in skeletal muscle. Cell Metab. *19*, 1034–1041.

Pollak, N., Dölle, C., and Ziegler, M. (2007). The power to reduce: pyridine nucleotides – small molecules with a multitude of functions. Biochem. J. *402*, 205–218.

Powanda, M.C., and Wannemacher, R.W., Jr. (1970). Evidence for a linear correlation between the level of dietary tryptophan and hepatic NAD concentration and for a systematic variation in tissue NAD concentration in the mouse and the rat. J. Nutr. *100*, 1471–1478.

Ratajczak, J., Joffraud, M., Trammell, S.A., Ras, R., Canela, N., Boutant, M., Kulkarni, S.S., Rodrigues, M., Redpath, P., Migaud, M.E., et al. (2016). NRK1 controls nicotinamide mononucleotide and nicotinamide riboside metabolism in mammalian cells. Nat. Commun. *7*, 13103.

Rechsteiner, M., Hillyard, D., and Olivera, B.M. (1976a). Magnitude and significance of NAD turnover in human cell line D98/AH2. Nature *259*, 695–696.

Rechsteiner, M., Hillyard, D., and Olivera, B.M. (1976b). Turnover at nicotinamide adenine dinucleotide in cultures of human cells. J. Cell Physiol. *88*, 207–217.

Revollo, J.R., Korner, A., Mills, K.F., Satoh, A., Wang, T., Garten, A., Dasgupta, B., Sasaki, Y., Wolberger, C., Townsend, R.R., et al. (2007). Nampt/PBEF/visfatin regulates insulin secretion in β cells as a systemic NAD biosynthetic enzyme. Cell Metab. *6*, 363–375.

Rouleau, M., Patel, A., Hendzel, M.J., Kaufmann, S.H., and Poirier, G.G. (2010). PARP inhibition: PARP1 and beyond. Nat. Rev. Cancer *10*, 293–301.

Ryu, D., Zhang, H., Ropelle, E.R., Sorrentino, V., Mazala, D.A., Mouchiroud, L., Marshall, P.L., Campbell, M.D., Ali, A.S., Knowels, G.M., et al. (2016). NAD+ repletion improves muscle function in muscular dystrophy and counters global PARylation. Sci. Transl. Med. *8*, 361ra139.

Sahar, S., Nin, V., Barbosa, M.T., Chini, E.N., and Sassone-Corsi, P. (2011). Altered behavioral and metabolic circadian rhythms in mice with disrupted NAD+ oscillation. Aging (Albany, NY) *3*, 794–802.

Sauve, A.A., and Schramm, V.L. (2003). Sir2 regulation by nicotinamide results from switching between base exchange and deacetylation chemistry. Biochemistry *42*, 9249–9256.

Sauve, A.A., Munshi, C., Lee, H.C., and Schramm, V.L. (1998). The reaction mechanism for CD38. A single intermediate is responsible for cyclization, hydrolysis, and base-exchange chemistries. Biochemistry *37*, 13239–13249.

Schreiber, V., Dantzer, F., Ame, J.C., and de Murcia, G. (2006). Poly(ADP-ribose): novel functions for an old molecule. Nat. Rev. Mol. Cell Biol. *7*, 517–528.

Soetaert, K., Petzoldt, T., and Setzer, R.W. (2010). Package deSolve: solving initial value differential equations in R. J. Stat. Softw. *33*, 1–25.

Su, X., Lu, W., and Rabinowitz, J.D. (2017). Metabolite spectral accuracy on orbitraps. Anal. Chem. *89*, 5940–5948.

Trammell, S.A., and Brenner, C. (2013). Targeted, LCMS-based metabolomics for quantitative measurement of NAD(+) metabolites. Comput. Struct. Biotechnol. J. *4*, e201301012.

Trammell, S.A., Schmidt, M.S., Weidemann, B.J., Redpath, P., Jaksch, F., Dellinger, R.W., Li, Z., Abel, E.D., Migaud, M.E., and Brenner, C. (2016). Nicotinamide riboside is uniquely and orally bioavailable in mice and humans. Nat. Commun. *7*, 12948.

van de Ven, R.A.H., Santos, D., and Haigis, M.C. (2017). Mitochondrial sirtuins and molecular mechanisms of aging. Trends Mol. Med. *23*, 320–331.

Virág, L., Robaszkiewicz, A., Rodriguez-Vargas, J.M., and Oliver, F.J. (2013). Poly(ADP-ribose) signaling in cell death. Mol. Aspects Med. *34*, 1153–1167.

Wang, J., Zhai, Q., Chen, Y., Lin, E., Gu, W., McBurney, M.W., and He, Z. (2005). A local mechanism mediates NAD-dependent protection of axon degeneration. J. Cell Biol. *170*, 349–355.

Wang, J., Kim, T.H., Ahn, M.Y., Lee, J., Jung, J.H., Choi, W.S., Lee, B.M., Yoon, K.S., Yoon, S., and Kim, H.S. (2012). Sirtinol, a class III HDAC inhibitor, induces apoptotic and autophagic cell death in MCF-7 human breast cancer cells. Int. J. Oncol. *41*, 1101–1109.

Wang, T.T.Y., Schoene, N.W., Kim, E.K., and Kim, Y.S. (2013). Pleiotropic effects of the sirtuin inhibitor sirtinol involves concentration-dependent modulation of multiple nuclear receptor-mediated pathways in androgen-responsive prostate cancer cell LNCaP. Mol. Carcinog *52*, 676–685.

Wang, G., Han, T., Nijhawan, D., Theodoropoulos, P., Naidoo, J., Yadavalli, S., Mirzaei, H., Pieper, A.A., Ready, J.M., and McKnight, S.L. (2014). P7C3 neuroprotective chemicals function by activating the rate-limiting enzyme in NAD salvage. Cell *158*, 1324–1334.

Xiao, Y., Elkins, K., Durieux, J.K., Lee, L., Oeh, J., Yang, L.X., Liang, X., DelNagro, C., Tremayne, J., Kwong, M., et al. (2013). Dependence of tumor cell lines and patient-derived tumors on the NAD salvage pathway renders them sensitive to NAMPT inhibition with GNE-618. Neoplasia *15*, 1151–1160.

Yang, Y., and Sauve, A.A. (2016). NAD+ metabolism: bioenergetics, signaling and manipulation for therapy. Biochim. Biophys. Acta *1864*, 1787–1800.

Yuan, J., Bennett, B.D., and Rabinowitz, J.D. (2008). Kinetic flux profiling for quantitation of cellular metabolic fluxes. Nat. Protoc. *3*, 1328–1340.

Yuan, J., Doucette, C.D., Fowler, W.U., Feng, X.J., Piazza, M., Rabitz, H.A., Wingreen, N.S., and Rabinowitz, J.D. (2009). Metabolomics-driven quantitative analysis of ammonia assimilation in *E. coli*. Mol. Syst. Biol. *5*, 302.

Zerp, S.F., Vens, C., Floot, B., Verheij, M., and van Triest, B. (2014). NAD+ depletion by APO866 in combination with radiation in a prostate cancer model, results from an in vitro and in vivo study. Radiother. Oncol. *11*, 348–354.

Zhao, Y.J., Zhu, W.J., Wang, X.W., Zhang, L.H., and Lee, H.C. (2015). Determinants of the membrane orientation of a calcium signaling enzyme CD38. Biochim. Biophys. Acta *1853*, 2095–2103.

Zhou, W., Ni, T.K., Wronski, A., Glass, B., Skibinski, A., Beck, A., and Kuperwasser, C. (2016). The SIRT2 deacetylase stabilizes slug to control malignancy of basal-like breast cancer. Cell Rep. *17*, 1302–1317.

Zong, W.X., Ditsworth, D., Bauer, D.E., Wang, Z.Q., and Thompson, C.B. (2004). Alkylating DNA damage stimulates a regulated form of necrotic cell death. Genes Dev. *18*, 1272–1282.

STAR★METHODS

KEY RESOURCES TABLE

REAGENT or RESOURCE	SOURCE	IDENTIFIER
Antibodies		
Rabbit polyclonal α-PAR	Trevigen	Cat. #4336-BPC-100; RRID: AB_2721257
Goat polyclonal α-β actin	Abcam	Cat. # ab8229; RRID: AB_306374
Chemicals, Peptides, and Recombinant Proteins		
Olaparib	Selleck Chemicals	Cat. #S1060; CAS 763113-22-0
FK866	Cayman Chemical	Cat. 13287; CAS 658084-64-1
Sirtinol	Sigma	Cat. #S7942; CAS 410536-97-9
EX527	Sigma	Cat. #E7034; CAS 49843-98-3
Zeocin	Invitrogen	Cat. #ant-zn-1; CAS 11006-33-0
Gallotannin	Sigma	Cat. #1643328; CAS 1401-55-4
$[2,4,5,6-^2H]$NAM	Cambridge Isotope Laboratories	Cat. #DLM-6883-PK; CAS 347841-88-7
$[U-^{13}C]$Trp	Cambridge Isotope Laboratories	Cat. #CLM-4290-H-PK
$[U-^{13}C]$NA	Sigma	Cat. #595825; CAS 1189954-79-7
Experimental Models: Cell Lines		
MCF7	ATCC	HTB-22D
T47D	ATCC	HTB-133
MDA-MB-231	ATCC	HTB-26
MDA-MB-468	ATCC	HTB-132
HepG2	ATCC	HB-8065
Panc1	ATCC	CRL-1469
HCT116	ATCC	CCL-247
SK-MEL-2	ATCC	HTB-68
SK-MEL-28	ATCC	HTB-72
C2C12	ATCC	CRL-1772
Experimental Models: Organisms/Strains		
Mouse C57BL/6 pre-catheterized on the right jugular vein	Charles River Laboratories	Cat. #027JUGVEIN w BUTONVAB62BS
Software and Algorithms		
MAVEN software	http://genomics-pubs.princeton.edu/mzroll/index.php	N/A
Metabolic flux analysis	https://github.com/XiaoyangSu/NAD-fluxes	N/A

CONTACT FOR REAGENT AND RESOURCE SHARING

Further information and requests for resources and reagents should be directed to and will be fulfilled by the Lead Contact, Joshua Rabinowitz (joshr@princeton.edu).

EXPERIMENTAL MODEL AND SUBJECT DETAILS

Mice

Animal studies followed protocols approved by the Princeton University Institutional Animal Care and Use Committee. C57BL/6 mice pre-catheterized on the right jugular vein were purchased from Charles River Laboratories (Wilmington, MA). The mice were on 5053 lab rodent diet 20 (23.4% protein), and were housed in a temperature-controlled facility on normal light cycle (8 AM – 8 PM). *In vivo* infusion was performed on 12-14 week old female C57BL/6 mice. The mouse infusion setup (Instech Laboratories, Plymouth Meeting, PA) included a tether and swivel system so that the animal had free movement in the cage.

Cell Culture

Cell culture was performed in an atmosphere of 5% CO_2 at 37°C. The cancer cell lines (MCF7, T47D, MDA-MB-231, MDA-MB-468, HepG2, Panc1, 8988T, HCT116, SK-MEL-2 and SK-MEL-28) were obtained from the American Type Culture Collection (ATCC, Manassas, VA). XPA-restored and XPA-deficient cell lines were a kind gift of Dr. Vilhelm A. Bohr's lab (Fang et al., 2014). Cancer cells and XPA cells were grown in Dulbecco's modified eagle media (DMEM, Cellgro, 10-017) with 10% FBS (Sigma). Cells were switched to 10% dialyzed FBS (Sigma) 2 days before labeling experiments. 3T3-L1 pre-adipocytes were obtained from ATCC and differentiated as reported (Liu et al., 2016). Briefly, adipogenesis was induced in 3T3-L1 preadipocytes with a cocktail containing 5 μg/ml insulin, 0.5 mM isobutylmethylxanthine, 1 μM dexamethasone and 5 μM troglitazone (Sigma-Aldrich). After 2 d, new medium was added and cells were maintained in 5 μg/ml insulin. C2C12 cell line was obtained from ATCC, maintained in DMEM supplemented with 20% FBS, and differentiated with DMEM containing 2% donor equine serum (GE Healthcare Life Sciences) and 1 μM insulin (Sigma). Mouse primary hepatocytes were cultured in William's medium E supplemented with ITS (BD Biosciences) and dexamethasone (He et al., 2014), and were transferred into isotopic medium 12 h after implantation. Cell number was determined with an automatic cell counter (Invitrogen). Packed cell volume was determined with PCV tubes (TPP). MCF7, T47D, MDA-MB-231, MDA-MB-468, 8988T, XPA-restored and XPA-deficient cell lines were obtained from female subjects. HepG2, Panc1, HCT116, SK-MEL-2 and SK-MEL-28 were obtained from male subjects. 3T3-L1 and C2C12 were obtained from mouse (no information on gender).

METHOD DETAILS

siRNAs, Antibodies, and Drugs

siRNA of QPRT (sc-62914) and control siRNA were obtained from Santa Cruz. PA. The antibodies against the following proteins for western blot were purchased: PAR (Trevigen, 4336-BPC-100, 1:1000 dilution) and β-actin (Abcam, ab8229, 1:2000 dilution). The following drugs for perturbing NAD synthesis or consumption were purchased: FK866 (Cayman Chemical, 13287, 100nM), olaparib (10 μM), sirtinol (Sigma, S7942, 20 μM), EX527 (Sigma, E7034, 10 μM), zeocin (Invitrogen, 1360033, 250 μg per ml) and gallotannin (Sigma, 1643328, 100 μM). PAR in cellular lysates was detected as described (Krukenberg et al., 2014). Briefly, PAR antibody-conjugated beads (MagPlex-10H) and lysate were incubated together overnight at 4°C, and analyzed on the FlexMap3D (Luminex) after biotin and streptavidin conjugation.

Isotope Labeling

[2,4,5,6-^{2}H]NAM and [U-^{13}C]Trp were from Cambridge Isotope Laboratories and [U-^{13}C]NA was from Sigma. Isotopic NR (nicotinamide 7-^{13}C, ribose 2-^{2}H) was synthesized as described (Trammell et al., 2016). Briefly, D-[2-^{2}H]ribose (Omicron Biochemicals) was converted to labeled D-ribofuranose-tetraacetate, which was then used together with [7-^{13}C]NAM to synthesize isotopic NR. Unlabeled compounds (NAM, NA, Trp, β-Nicotinamide mononucleotide, NAD, NADH, NADP and NADPH) were purchased from Sigma. DMEM with isotopic NAM was prepared from scratch following the standard DMEM formula except without NAM and supplemented with isotopic NAM (32 μM). Isotope-labeled tryptophan medium was prepared from scratch following the standard DMEM formula except without tryptophan (and also, for Figure S1A only, NAM) and supplemented with isotopic tryptophan (80 μM). Isotopic medium was supplemented with 10% dialyzed FBS, except for C2C12 cells, where 2% donor equine serum was used instead.

Intravenous Infusion of Wild Type C57BL/6 Mice

In vivo infusion was performed on C57BL/6 mice pre-catheterized on the right jugular vein, at the room temperature of 21°C. Isotope-labeled metabolites were prepared as solutions in normal saline (100 mM for [U-^{13}C]Trp, 4 mM for [2,4,5,6-^{2}H]NAM, 0.2 mM for [U-^{13}C]NA) and infused via the catheter at a constant rate of 1 μL per 20 g per min. Blood samples (~20 μl) were collected by tail bleeding, placed on ice in the absence of anticoagulant, and centrifuged at 16,000g for 5 min at 4°C to isolate serum. At the end of the infusion, the mouse was euthanized by cervical dislocation and tissues were quickly dissected and snap frozen in liquid nitrogen with pre-cooled Wollenberger clamp. Serum and tissue samples were kept at -80°C before metabolite extraction for mass spectrometry analysis.

Metabolite Measurements in Cell Lines

Cells were grown in 6-well plates (Corning), and transferred into isotopic medium with 10% dialyzed FBS, which was refreshed daily for labeling experiments > 24 h. For steady state labeling of metabolites, labeled medium was replaced every day, and additionally 2 h before extracting metabolites. Metabolism was quenched and metabolites were extracted by aspirating media and immediately adding 1 mL -80°C 80:20 methanol: water. For intracellular metabolites which are present in medium (i.e. NAM, tryptophan), cells were washed with 37°C phosphate buffered saline for 3 times before adding -80°C 80:20 methanol: water. After 20 min of incubation on dry ice, the resulting mixture was scraped, collected into a centrifuge tube, and centrifuged at 10,000 g for 5 min at 4°C. The supernatants were analyzed within 24 h by liquid chromatography coupled to a mass spectrometer (LC-MS).

The LC–MS method involved hydrophilic interaction chromatography (HILIC) coupled to the Q Exactive PLUS mass spectrometer (Thermo Scientific). The LC separation was performed on a XBridge BEH Amide column (150 mm × 2.1 mm, 2.5 μm particle size, Waters, Milford, MA). Solvent A is 95%: 5% H_2O: acetonitrile with 20 mM ammonium bicarbonate, and solvent B is acetonitrile.

The gradient was 0 min, 85% B; 2 min, 85% B; 3 min, 80% B; 5 min, 80% B; 6 min, 75% B; 7 min, 75% B; 8 min, 70% B; 9 min, 70% B; 10 min, 50% B; 12 min, 50% B; 13 min, 25% B; 16 min, 25% B; 18 min, 0% B; 23 min, 0% B; 24 min, 85% B; 30 min, 85% B. Other LC parameters are: flow rate 150 μl/min, column temperature 25°C, injection volume 5 μL. The mass spectrometer was operated in positive ion mode for the detection of NAM and NR, and negative ion mode for other metabolites. Other MS parameters are: resolution of 140,000 at m/z 200, automatic gain control (AGC) target at 3e6, maximum injection time of 30 ms and scan range of m/z 75-1000. All isotope labeling patterns were corrected for natural abundance using AccuCor (Su et al., 2017), which uses matrix algebra (coded in R) to correct labeling data for both isotope natural abundance and tracer isotopic impurities. AccuCor calculates the correction matrices based on only non-resolved isotopic peaks, and therefore is suitable for high-resolution mass spectrometry data. AccuCor is a software freely available at https://github.com/XiaoyangSu/Isotope-Natural-Abundance-Correction.

Metabolite Measurements of Serum and Tissues

Serum was thawed on ice before adding -80°C 80:20 methanol: water with a volume of 20 μL solvent per μL serum, vortexed, incubated on ice for 10 min, and centrifuged at 16,000 g for 10 min, with the supernatant used for LC-MS analysis. Frozen tissues were weighed, ground with a cryomill (Retsch) at 25 Hz for 30 seconds before adding -20°C tissue extraction solution (40:40:20 acetonitrile: methanol: water) with a volume of 40 μL solvent per mg tissue, and incubated on ice for 20 min. Tissue samples were then centrifuged at 16,000 g for 20 min. The supernants were transferred to new tubes and centrifuged again at 16,000 g for 20 min to remove any residual debris before analysis. To obtain absolute metabolite concentrations, internal standards (unlabeled NAD, NADH, NADP, NADPH, NAM) were added directly to the initial quenching and extraction solvent. Supernatants were analyzed within 24 h by LC-MS.

QUANTIFICATION AND STATISTICAL ANALYSIS

Quantification of NAD Synthesis Fluxes in Cell Lines

After switching to medium with labeled NAM, the cellular NAM is almost completely labeled within the first hour (Figure 1B, left). For simplicity, we treat the labeling of cellular NAM as if it occurred instantaneously at t=0. The unlabeled fraction of NAD (NAD$_U$, Figure 1B) decreases as

$$\frac{dNAD_U(t)}{dt} = -\frac{f_{in}}{[NAD]} NAD_U(t) \qquad \text{(Equation 2)}$$

where f_{in} is the total NAD synthesis flux and [NAD] is the sum of intracellular NAD and NADH concentration. The kinetic equation for the unlabeled fraction is given by the solution to Equation 2, i.e.,

$$NAD_U(t) = e^{-\frac{f_{in}}{[NAD]} \cdot t} \qquad \text{(Equation 3)}$$

The best estimation of f_{in} was acquired by minimizing the deviation of the model-predicted NAD$_U$ and the measured values. For example, in the case of Figure 1B (T47D cells), this fitting yields a value of 0.077 h^{-1} for the rate constant $f_{in}/[NAD]$ (corresponding to a turnover half time $t_{1/2} \approx 9$ hr). Since [NAD] in T47D cells is 1880 pmol per million cells, we then obtained f_{in} to be 144 pmol per million cells per hour. 95% CI was determined by Monto Carlo method. In each iteration, all [NAD$_U$] were randomly generated according to a t-distribution with measured mean and variance. The optimal f_{in} was calculated for each of 200 iterations. The reported CI is the central 95% region of the resulting f_{in} distribution.

Due to the exponential growth of the cells, part of this total NAD synthesis flux goes to pool expansion. The growth demand f_{growth} was determined by growth and NAD pool (Equation 4).

$$f_{growth} = g \cdot [NAD] \qquad \text{(Equation 4)}$$

where g is the growth rate constant, determined by cell number (N) measurement over time $dN/dt = gN$. For T47D cells, $g = 0.015$ h^{-1} (corresponding to a doubling time of 46 h). Growth rates were calculated using the software package Origin by fitting to an exponential, as mean ± 95% confidence interval. We thus get f_{growth} 28± 2 pmol per million cells per hour, which is approximately 20% of the total NAD synthesis flux. The gap between f_{in} and f_{growth}, 118 pmol per million cells per hour, is the NAD consumption flux.

Quantification of NAD Consumption Fluxes in Cell Lines

To quantify the NAD consumption flux by NAD kinase (f_{NADK}), we note that after switching to medium with labeled NAM the labeled fraction of NADP (NADP$_L$) follows

$$\frac{dNADP_L(t)}{dt} = (NAD_L(t) - NADP_L(t)) \cdot \frac{f_{NADK}}{[NADP]} \qquad \text{(Equation 5)}$$

where the kinetics of NAD$_L$(t) is given by

$$\frac{dNAD_L(t)}{dt} = \frac{f_{in}}{[NAD]} (1 - NAD_L(t)) \qquad \text{(Equation 6)}$$

[Equation 5](#) can be solved analytically, implying a unique flux solution ([Yuan et al., 2008](#)). Best estimation of f_{NADK} is obtained by minimizing the deviation of the calculated $NADP_L$ and the measured values. $NADP_L(t)$ can be calculated from [Equations 5](#) and [6](#) with previously determined f_{in} (144 pmol per million cells per hour), measured [NAD] (constant total intracellular NAD and NADH concentration, 1880 pmol per million cells) and [NADP] (constant total intracellular NADP and NADPH concentration, 84 pmol per million cells). 95% CI was determined by Monto Carlo method. In each iteration, all the $NADP_L$ were randomly generated according to a t-distribution based on the measured mean and variance. The optimal f_{NADK} was calculated for each of 200 iterations. The reported CI is the central 95% region of the resulting f_{NADK} distribution.

To calculate consumption fluxes by PARPs and Sirtuins, we blocked the fluxes with their respective inhibitors while switching to labeled medium, and followed the labeling kinetics. As the inhibitor does not affect the synthesis flux f_{in} (based on experimental data showing that accumulation of labeled is unaltered), we model the labeled NAD pool ($[NAD_L]$) and unlabeled NAD pool ($[NAD_U]$) as

$$\frac{d[NAD_L]}{dt} = f_{in} - \frac{[NAD_L]}{[NAD_L] + [NAD_U]} \cdot f_{out} \qquad \text{(Equation 7)}$$

and

$$\frac{d[NAD_U]}{dt} = - \frac{[NAD_U]}{[NAD_L] + [NAD_U]} \cdot f_{out} \qquad \text{(Equation 8)}$$

Since the initial conditions are known ($[NAD_U](t=0) = [NAD]$, $[NAD_L](t=0) = 0$), with previously determined f_{in} (144 pmol per million cells per hour), $[NAD_L](t)$ and $[NAD_U](t)$ can be calculated for any assumed value of f_{out}. The best estimation of f_{out} is acquired by minimizing the deviation of model predicted $[NAD_L]$ and $[NAD_U]$ and the measured values. 95% CI was determined by Monto Carlo method. In each of iteration, all the $[NAD_L]$ and $[NAD_U]$ were randomly generated according to a t-distribution with measured mean and variance. The optimal f_{out} was calculated for each of 200 iterations. The reported CI is the central 95% region of the resulting f_{out} distribution.

Quantification of NAD Fluxes *In Vivo*

We infused $[U-^{13}C]$Trp (Trp_{11}, all 11 carbons are labeled), $[U-^{13}C]$NA (NA_6, all 6 carbons are labeled) and $[2,4,5,6-^2H]$NAM (NAM_4, nicotinamide with all hydrogen on the ring labeled) separately to mice to determine fluxes. Both Trp_{11} and NA_6 result in NAD_6 (NAD with all carbons on the nicotinamide part labeled) and then $NAM_{Tissue,6}$. $NAM_{Tissue,6}$ is released to the circulation ($NAM_{Serum,6}$) before being taken by tissues to remake NAD. NAD_3 is made directly from NAM_4 (one deuteron of NAM_4 becomes the redox-active deuteron of NAD and thus is quickly lost). Breakdown of NAD_3 yields NAM_3.

In each organ, as shown in [Figures 5](#)B and [4](#) NAD metabolic fluxes are calculated assuming metabolic steady state in each tissue: f_1 is NAD *de novo* synthesis flux from tryptophan, f_2 is NAD synthesis flux from NA, f_3 is NAD synthesis from tissue nicotinamide (NAM), and f_4 is the flux of NAM being taken up from serum. At metabolic steady state, the NAD and nicotinamide concentrations in tissue stay constant. By mass balance, the corresponding breakdown (NAD → NAM) and excretion (tissue NAM → circulation) fluxes are fully determined by the production fluxes above, and thus are not included as separate variables in the model. The following set of differential equations are used to calculate the tissue NAD and NAM labeling patterns at each time point.

$$f_1(Trp_{11} - NAD_6) + f_2(NA_6 - NAD_6) + f_4 \qquad \text{(Equation 9)}$$

In the equations, NAD_i represent the labeling fraction of mass isotopomer M+i of tissue NAD. $NAM_{Tissue\ i}$ and $NAM_{Serum\ i}$ represent the labeling fraction of tissue NAM and serum NAM M+i, respectively. Trp_{11} and NA_6 represent the labeling fraction of serum tryptophan and serum NA, respectively. c_{NAD} and c_{NAM} are tissue concentrations of NAD(H) and NAM, respectively (in nmol/gram tissue weight).

Tryptophan and NA reached steady state in serum within 30 min, therefore Trp_{11} and NA_6 were treated as constants (60% and 85%, respectively). Serum NAM labeling changes as a function of time. In our differential equations, serum NAM labeling is treated as a known input: the serum NAM labeling was measured at multiple time points, and the labeling data were fit to an empirically determined function ([Figure S6](#)A). At t=0, NAD_{M+0}, NAM_{M+0} and $NADPH_{M+0}$ are 1, while all other fractions are 0. The tissue specific concentration of NAM and NAD was measured by LC-MS. For any given set of the four fluxes, the dynamic labeling patterns can be calculated from the differential equations. The calculated values were then compared to the measured labeling patterns (1 h, 2 h, 5 h during $[2,4,5,6-^2H]$NAM infusion, 5 h after $[U-^{13}C]$Trp infusion, 5 h after $[U-^{13}C]$NA infusion). The best estimated flux set is achieved by minimizing the variance-normalized sum of squared deviation (Var-SSR) between the calculated labeling patterns and the measured ones. The normalization was by weighing the observed deviation of each measurement by the average (across time points and conditions) standard deviation of replicate experimental labeling data for that species: 1.5% for NAM and 0.8% for NAD (these values refer to the absolute error of the labeled fraction, for example, for a NAM M+3 fraction of 10%, the range ± 1 SD is 8.5% to 11.5%). The numerical simulation of the differential equations were performed in R with the deSolve package and the optimization was performed with minqa package ([Soetaert et al., 2010](#)). 95% confidence intervals were estimated by (i) starting from the best-scoring flux distribution, (ii) changing the specific flux, (iii) choosing a combination of other fluxes which give minimal increase in the Var-SSR, (iv) determining the increase in the objective function Var-SSR and using an increase of 3.84 as the cutoff for 95% confidence interval ([Antoniewicz et al., 2006](#)). The goodness of fit was evaluated by chi-square test, $\chi^2_{0.05}(df=15)=25$. The 15 degrees of freedom are based on our having obtained 19 measurements (different labeled forms of NAM and NAD at multiple time points for

different nutrient infusions) and having 4 unknown fluxes (i.e. 4 degree of freedom); 19 - 4=15. See Table S5 for the sum of squared residuals (SSR) value for every tissue.

As a validation of the flux estimation, the optimal set of fluxes determined as above were used to simulate (without any free parameters) the labeling pattern of tissue NAM and NAD upon co-infusion of [U-^{13}C]Trp combined with [2,4,5,6-^{2}H]NAM, and separately of [U-^{13}C]NA combined with [2,4,5,6-^{2}H]NAM, where the same doses tracers were used as for the individual tracing experiments (5 nmol per gram per min for [U-^{13}C]Trp, 0.2 nmol per gram per min for [2,4,5,6-^{2}H]NAM, 0.02 nmol per gram per min for [U-^{13}C]NA). The simulated labeling data were then compared to the experimentally measured values (see Tables S6 and S7).

Statistical Analysis

Data are displayed as mean ± SE. In figures, asterisks denote statistical significance as calculated by a two-tailed unpaired Student's t-test (*, $p < 0.05$; **, $p < 0.01$). This test is appropriate for determining whether the means of two populations are equal. Data were not tested for the assumptions of normality and equal variance across groups. Linear regression was used to test for the linear relationships between variables. Exponential curve fitting was used to test whether data followed an exponential decay pattern. Statistical parameters are reported in the Figures and Figure Legends. $P<0.05$ was considered statistically significant. N represents the number of replicates.

DATA AND SOFTWARE AVAILABILITY

The code for metabolic flux analysis of *in vivo* NAD metabolism is available at https://github.com/XiaoyangSu/NAD-fluxes.

Supplemental Information

Quantitative Analysis of NAD

Synthesis-Breakdown Fluxes

Ling Liu, Xiaoyang Su, William J. Quinn III, Sheng Hui, Kristin Krukenberg, David W. Frederick, Philip Redpath, Le Zhan, Karthikeyani Chellappa, Eileen White, Marie Migaud, Timothy J. Mitchison, Joseph A. Baur, and Joshua D. Rabinowitz

Table S1. NAD precursor availability in DMEM, mouse chow, the serum of mice, and circulatory turnover fluxes (F_{circ}). Related to Figure 1, Figure 5 and STAR Methods. DMEM and chow data are from the manufacturer. Serum data are LC-MS measurements made here (mean ± s.d., n = 3). Turnover fluxes were calculated from infusion rate and steady state labeling percentage(Hui *et al.*, 2017) (mean ± s.d., n = 3).

	Concentrations			Turnover fluxes
	DMEM	Mouse chow	Mouse serum	F_{circ}
Trp	80 μM	13.7 mM	46±4 μM	2.8±0.4 nmol/g/min
NAM	32 μM	-	2.1±0.2 μM	0.55±0.04 nmol/g/min
NA	-	0.98 mM	0.22±0.07 μM	2.0±0.9 pmol/g/min
NMN	-	-	1nM	-
NAD	-	-	< 1nM	-
NR	-	-	7.0±2.3 nM	-

Table S2. NAD fluxes and protein PARrylation across five human breast cancer cell lines. Related to Figure 3. Data for lysate PARylation (detected as described(Krukenberg *et al.*, 2014)) are mean ± s.d., n = 6. Data for NAD concentration are mean ± s.d., n = 3. Data for labeling $t_{1/2}$ and PARP-mediated consumption are mean ± 95% confidence interval (L.B. lower boundary, U.B. upper boundary).

		KPL1	MCF7	AU565	T47D	SKBR3
Lysate PARylation (ug PAR per mg protein)		61±10	39±8	2.9±0.7	2.1±0.6	1.4±0.5
NAD pool (nmol per million cells)		2.1±0.3	4.0±0.2	4.3±0.2	1.9±0.2	2.6±0.4
NAD labeling $t_{1/2}$ (h)		12.2±0.7	13.5±0.4	9.7±0.5	8.6±0.3	9.9±0.5
NAD consumption by PARP (pmol per million cells per h)	Best	17	53	56	38	48
	L.B.	14	46	44	28	38
	U.B.	25	55	60	43	55

Table S3. Half-time for NAD labeling by ^{2}H-NAM and for NAD depletion upon adding FK866 (100 nM) in different cell lines. Related to Figure 4. Data are mean ± 95% confidence interval.

hour	Breast Cancer				GI Cancer				Melanoma		Differentiation	
	MDA-MB-231	MDA-MB-468	MCF7	T47D	HCT116	HepG2	Panc1	8988T	SK-MEL-2	SK-MEL-28	C2C12	3T3-L1
NAD labeling halflife	7.1 ±1.2	5.6 ±0.4	13.2 ±0.3	8.5 ±0.6	6.6 ±0.6	8.1 ±0.3	12.3 ±2.5	10.2 ±0.4	12.9 ±0.5	7.3 ±0.8	8.3 ±1.2	5.1 ±0.3
Time to deplete half NAD	7.3 ±0.3	4.9 ±0.3	13.2 ±0.9	6.4 ±0.2	7.1 ±0.9	7.3 ±0.7	11.9 ±1.0	7.4 ±0.6	11.2 ±1.0	7.9 ±1.4	8.3 ±0.8	5.9 ±0.6

Table S4. Concentrations of NAM, NAD(H), and NADP(H) in murine tissues. Related to Figure 5 and STAR Methods. Data are mean ± s.d., n = 4.

μM	White Adipose	Brain	Heart	Kideny	Liver	Lung	Pancreas	Skeletal Muscle	Small Intestine	Spleen
NAM	8±3	46±13	60±22	58±12	44±18	51±24	40±17	47±13	90±13	64±10
NAD(H)	35±9	258±53	459±47	518±42	690±48	146±21	467±59	219±53	241±43	255±35
NADP(H)	2.5±0.2	55±21	32±5	90±33	97±20	63±31	24±8	101±40	53±26	49±19

Table S5. Metabolic flux distributions (normalized to weight) with confidence intervals and SSR in tissues. Related to Figure 6. Fluxes are normalized to weight. The goodness of fit was evaluated by chi-square test, $\chi^2_{0.05}(df=15)=25$. Each flux is shown with 95% confidence intervals of NAD labeling half-lives (L.B. lower boundary, U.B. upper boundary).

Tissue		Flux (μM / h)				Half-life (h)	SSR
		f_1	f_2	f_3	f_4		
White Adipose	Best	0.0	0.1	2.3	10.7	2.3	38.2
	L.B.	0.0	0.1	2.3	8.1	3.0	
	U.B.	0.0	0.1	2.2	14.9	1.6	
Brain	Flux	0.0	0.1	17.1	46.0	3.9	20.6
	L.B.	0.0	0.1	17.0	37.4	4.8	
	U.B.	0.0	0.1	17.0	57.4	3.1	
Heart	Flux	0.0	1.0	21.0	120.5	2.6	21.6
	L.B.	0.0	1.0	20.7	90.5	3.5	
	U.B.	0.1	1.1	20.7	169.5	1.9	
Kidney	Flux	6.3	5.4	55.7	124.0	2.6	23.4
	L.B.	6.1	5.2	55.9	105.0	3.1	
	U.B.	6.6	5.5	54.8	148.0	2.2	
Lung	Flux	0.0	0.8	37.4	41.9	2.4	153.0
	L.B.	0.0	0.7	39.2	36.9	2.7	
	U.B.	0.0	0.8	35.7	47.7	2.1	
Skeletal Muscle	Flux	0.0	0.0	9.4	10.4	14.6	19.8
	L.B.	0.0	0.0	8.4	6.5	23.2	
	U.B.	0.0	0.0	10.1	14.7	10.3	
Pancreas	Flux	0.0	3.5	52.1	38.1	7.8	66.2
	L.B.	0.0	3.3	49.4	32.5	9.1	
	U.B.	0.0	3.7	54.1	44.3	6.8	
Small Intestine	Flux	0.0	1.2	73.6	581.6	0.3	99.3
	L.B.	0.0	1.1	76.1	435.6	0.4	
	U.B.	0.0	1.2	71.0	859.6	0.2	
Spleen	Flux	0.0	1.1	69.4	409.2	0.4	53.5
	L.B.	0.0	1.0	71.7	325.2	0.5	
	U.B.	0.0	1.1	67.0	547.2	0.3	
Liver	Flux	55.0	0.9	54.0	176.4	2.1	16.1
	L.B.	54.2	0.8	54.5	140.4	2.4	
	U.B.	55.7	1.0	52.1	228.4	1.7	

Table S6. Measured and model-predicted NAD and NAM labeling fractions in tissues, from co-infusion of [U-^{13}C]Trp and [2,4,5,6-^{2}H]NAM (20:1 ratio, equal to their physiological ratio in serum) for 5 h. Related to Figure 6. Correlation coefficient is 0.993. Measured data are mean ± s.d., n=3.

Tissue	Isotopic fraction	Simulated	Measured Mean	Measured s.d.	Tissue	Isotopic fraction	Simulated	Measured Mean	Measured s.d.
White Adipose	NAM M+0	0.894	0.849	0.010	Skeletal Muscle	NAM_0	0.853	0.724	0.012
	NAM M+3	0.044	0.078	0.009		NAM M+3	0.018	0.044	0.013
	NAM M+4	0.055	0.068	0.002		NAM M+4	0.118	0.220	0.011
	NAM M+6	0.007	0.006	0.002		NAM M+6	0.010	0.012	0.011
	NAD M+0	0.945	0.940	0.000		NAD M+0	0.983	0.987	0.009
	NAD M+3	0.051	0.059	0.007		NAD M+3	0.016	0.013	0.005
	NAD M+6	0.003	0.002	0.006		NAD M+6	0.001	0.000	0.014
Brain	NAM M+0	0.866	0.792	0.012	Pancreas	NAM M+0	0.757	0.764	0.010
	NAM M+3	0.040	0.046	0.009		NAM M+3	0.048	0.058	0.002
	NAM M+4	0.084	0.151	0.003		NAM M+4	0.176	0.139	0.008
	NAM M+6	0.010	0.011	0.000		NAM M+6	0.019	0.040	0.000
	NAD M+0	0.950	0.975	0.000		NAD M+0	0.946	0.949	0.000
	NAD M+3	0.047	0.025	0.001		NAD M+3	0.051	0.049	0.001
	NAD M+6	0.003	0.000	0.001		NAD M+6	0.003	0.002	0.000
Heart	NAM M+0	0.908	0.896	0.006	Small Intestine	NAM M+0	0.780	0.786	0.005
	NAM M+3	0.039	0.033	0.011		NAM M+3	0.169	0.159	0.012
	NAM M+4	0.047	0.064	0.005		NAM M+4	0.036	0.054	0.006
	NAM M+6	0.007	0.006	0.000		NAM M+6	0.015	0.012	0.001
	NAD M+0	0.956	0.975	0.012		NAD M+0	0.798	0.874	0.013
	NAD M+3	0.042	0.024	0.012		NAD M+3	0.189	0.120	0.013
	NAD M+6	0.003	0.001	0.001		NAD M+6	0.013	0.005	0.001
Kidney	NAM M+0	0.808	0.845	0.013	Spleen	NAM M+0	0.780	0.756	0.009
	NAM M+3	0.062	0.053	0.005		NAM M+3	0.159	0.094	0.001
	NAM M+4	0.093	0.068	0.010		NAM M+4	0.047	0.135	0.011
	NAM M+6	0.036	0.033	0.002		NAM M+6	0.015	0.015	0.000
	NAD M+0	0.888	0.940	0.001		NAD M+0	0.806	0.874	0.007
	NAD M+3	0.073	0.041	0.001		NAD M+3	0.182	0.122	0.006
	NAD M+6	0.040	0.019	0.000		NAD M+6	0.012	0.004	0.000
Lung	NAM M+0	0.764	0.782	0.013	Liver	NAM M+0	0.711	0.722	0.017
	NAM M+3	0.074	0.066	0.003		NAM M+3	0.049	0.024	0.002
	NAM M+4	0.146	0.139	0.011		NAM M+4	0.061	0.022	0.018
	NAM M+6	0.017	0.012	0.000		NAM M+6	0.180	0.232	0.002
	NAD M+0	0.878	0.908	0.011		NAD M+0	0.732	0.798	0.009
	NAD M+3	0.115	0.089	0.008		NAD M+3	0.049	0.030	0.001
	NAD M+6	0.007	0.003	0.006		NAD M+6	0.219	0.172	0.010

Table S7. Measured and model-predicted NAD and NAM labeling fractions in tissues, from co-infusion of [U-^{13}C]NA and [2,4,5,6-^{2}H]NAM (1:10 ratio, equal to their ratio in serum) for 5 h. Related to Figure 6. Correlation coefficient is 0.997. Measured data are mean ± s.d., n=3.

| Tissue	Isotopic fraction	Simulated	Measured		Tissue	Isotopic fraction	Simulated	Measured	
			Mean	s.d.				Mean	s.d.
White Adipose	NAM M+0	0.873	0.877	0.007	Skeletal Muscle	NAM M+0	0.832	0.857	0.000
	NAM M+3	0.061	0.078	0.009		NAM M+3	0.032	0.039	0.003
	NAM M+4	0.057	0.022	0.002		NAM M+4	0.132	0.099	0.007
	NAM M+6	0.009	0.023	0.003		NAM M+6	0.004	0.005	0.004
	NAD M+0	0.925	0.924	0.007		NAD M+0	0.979	0.974	0.007
	NAD M+3	0.065	0.065	0.010		NAD M+3	0.021	0.023	0.003
	NAD M+6	0.009	0.011	0.006		NAD M+6	0.001	0.002	0.003
Brain	NAM M+0	0.850	0.897	0.005	Pancreas	NAM M+0	0.727	0.755	0.009
	NAM M+3	0.058	0.068	0.008		NAM M+3	0.074	0.090	0.008
	NAM M+4	0.088	0.032	0.005		NAM M+4	0.181	0.127	0.009
	NAM M+6	0.004	0.004	0.000		NAM M+6	0.018	0.028	0.000
	NAD M+0	0.937	0.957	0.007		NAD M+0	0.908	0.898	0.003
	NAD M+3	0.061	0.041	0.007		NAD M+3	0.064	0.057	0.000
	NAD M+6	0.002	0.002	0.000		NAD M+6	0.028	0.044	0.003
Heart	NAM M+0	0.890	0.879	0.002	Small Intestine	NAM M+0	0.737	0.743	0.008
	NAM M+3	0.053	0.081	0.002		NAM M+3	0.212	0.202	0.005
	NAM M+4	0.048	0.014	0.003		NAM M+4	0.037	0.033	0.014
	NAM M+6	0.009	0.026	0.001		NAM M+6	0.014	0.022	0.001
	NAD M+0	0.939	0.943	0.000		NAD M+0	0.753	0.776	0.009
	NAD M+3	0.053	0.047	0.002		NAD M+3	0.233	0.209	0.006
	NAD M+6	0.009	0.011	0.001		NAD M+6	0.014	0.016	0.002
Kidney	NAM M+0	0.792	0.783	0.009	Spleen	NAM M+0	0.739	0.781	0.009
	NAM M+3	0.086	0.103	0.002		NAM M+3	0.201	0.185	0.001
	NAM M+4	0.095	0.062	0.001		NAM M+4	0.047	0.015	0.009
	NAM M+6	0.027	0.053	0.005		NAM M+6	0.013	0.018	0.000
	NAD M+0	0.874	0.851	0.002		NAD M+0	0.762	0.825	0.003
	NAD M+3	0.091	0.083	0.001		NAD M+3	0.224	0.160	0.002
	NAD M+6	0.034	0.066	0.001		NAD M+6	0.014	0.015	0.001
Lung	NAM M+0	0.730	0.819	0.006	Liver	NAM M+0	0.867	0.832	0.009
	NAM M+3	0.106	0.129	0.003		NAM M+3	0.066	0.063	0.001
	NAM M+4	0.152	0.030	0.011		NAM M+4	0.061	0.095	0.009
	NAM M+6	0.013	0.022	0.002		NAM M+6	0.006	0.010	0.000
	NAD M+0	0.837	0.876	0.005		NAD M+0	0.934	0.942	0.005
	NAD M+3	0.146	0.110	0.004		NAD M+3	0.061	0.046	0.004
	NAD M+6	0.017	0.014	0.002		NAD M+6	0.005	0.011	0.001
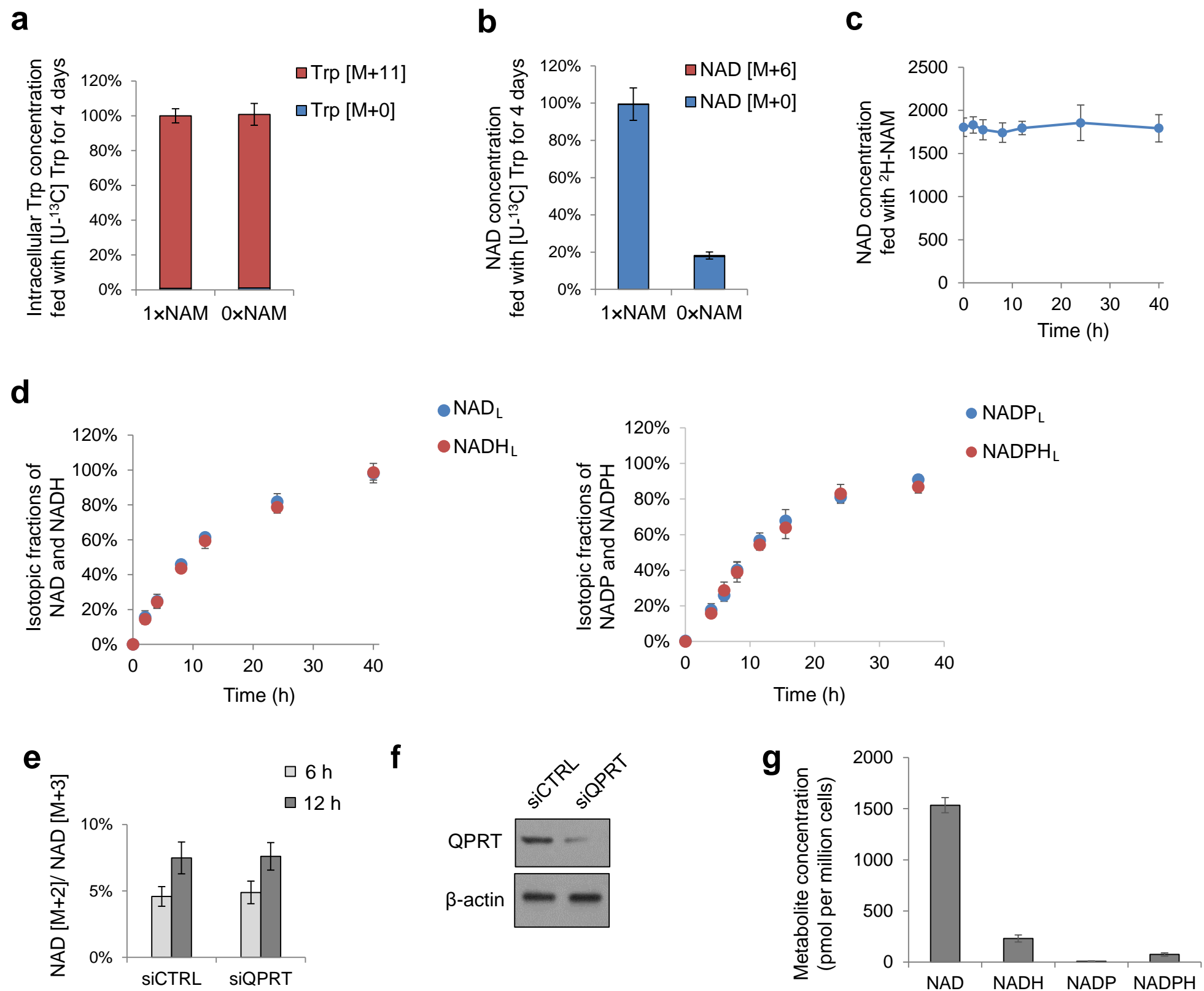
Figure S1. In T47D cells, there is not *de novo* NAD synthesis from tryptophan and NAD M+2 does not arise due to activity of the *de novo* pathway enzyme QPRT. Related to Figure 1 and Figure 2. **(a)** In cells grown in [U-^{13}C] Trp in normal DMEM (1x NAM) or NAM-free DMEM (0x NAM) for 4 days, intracellular tryptophan is essentially fully labeled. **(b)** NAD is not detectably labeled. Absolute signal intensity for Trp and NAD are normalized to the signal in standard DMEM. **(c)** NAD concentration in cells fed ^{2}H-NAM. **(d)** Indistinguishable labeling of NAD and NADH (left) and NADP and NADPH (right) in cells fed ^{2}H-NAM. **(e)** Knockdown of QPRT does not alter the ratio between NAD [M+2] and NAD [M+3] following 6 h or 12 h of ^{2}H-NAM labeling. **(f)** Western blot for QPRT knockdown. **(g)** Concentrations of NAD, NADH, NADP and NADPH. Data are mean $\pm$ s.d., n = 3.
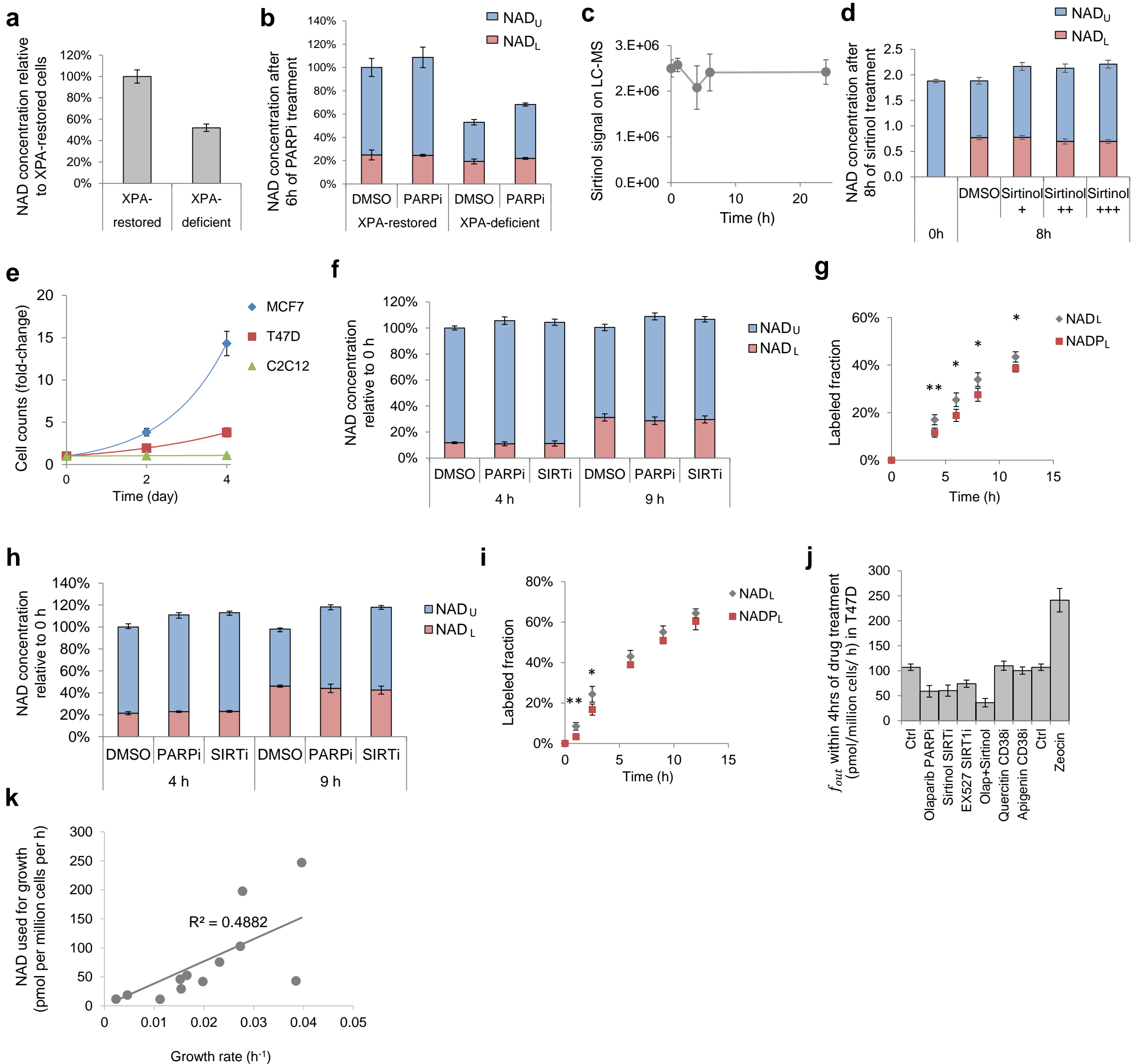
Figure S2. Role of growth, PARP, sirtuins, and CD38 in NAD turnover in selected cell types. Related to Figure 3. **(a)** NAD concentration in XPA-deficient or XPA-restored cells (relative to restored cells). **(b)** NAD concentration and labeling in XPA-deficient and XPA-restored cells treated with DMSO (negative control) or olaparib (10 μM, PARP1/2 inhibitor) for 6 h. Olaparib was added simultaneously with switching cells into ^{2}H-NAM. **(c)** Stability of 50 μM sirtinol in DMEM supplemented with 10% DFBS (37°C). **(d)** NAD concentration and labeling in T47D cells treated with DMSO (negative control), 25 μM sirtinol (+), 50 μM sirtinol (++), or 100 μM sirtinol (+++), for 8 h. Sirtinol was added simultaneously with switching cells into ^{2}H-NAM. **(e)** Growth rate of MCF7, T47D and differentiating C2C12 cells. Lines are single exponential fits. **(f)** Measurement of NAD consumption by PARPs and sirtuins in MCF7 cells. NAD concentration and labeling was measured in cells treated with DMSO, olaparib (10 μM), or sirtinol (25 μM) for 4 h or 9 h. Drug was added simultaneously with switching cells into ^{2}H-NAM. **(g)** Measurement of NAD consumption by NAD kinase in MCF7 cells. Cells were fed ^{2}H-NAM starting at t = 0 and NAD and NADP labeling were measured. NAD labeling significantly exceeded NADP labeling at early time points (**p<0.01, * p<0.05, paired t-test). **(h, i)** Same as (f, g) but in C2C12 cells. For panel a-i, data are mean $\pm$ s.d., n = 3. **(j)** CD38 does not consume substantial NAD in T47D cells. Consumption rates were calculated based on 4 h incubation with ^{2}H-NAM and quercetin (50μM, CD38 inhibitor) or apigenin (25μM, CD38 inhibitor). Bars are mean $\pm$ 95% confidence interval of f_{out}. **(k)** Across the same 12 cell lines as Figure 4, NAD usage for growth correlates with growth rate (p=0.01).
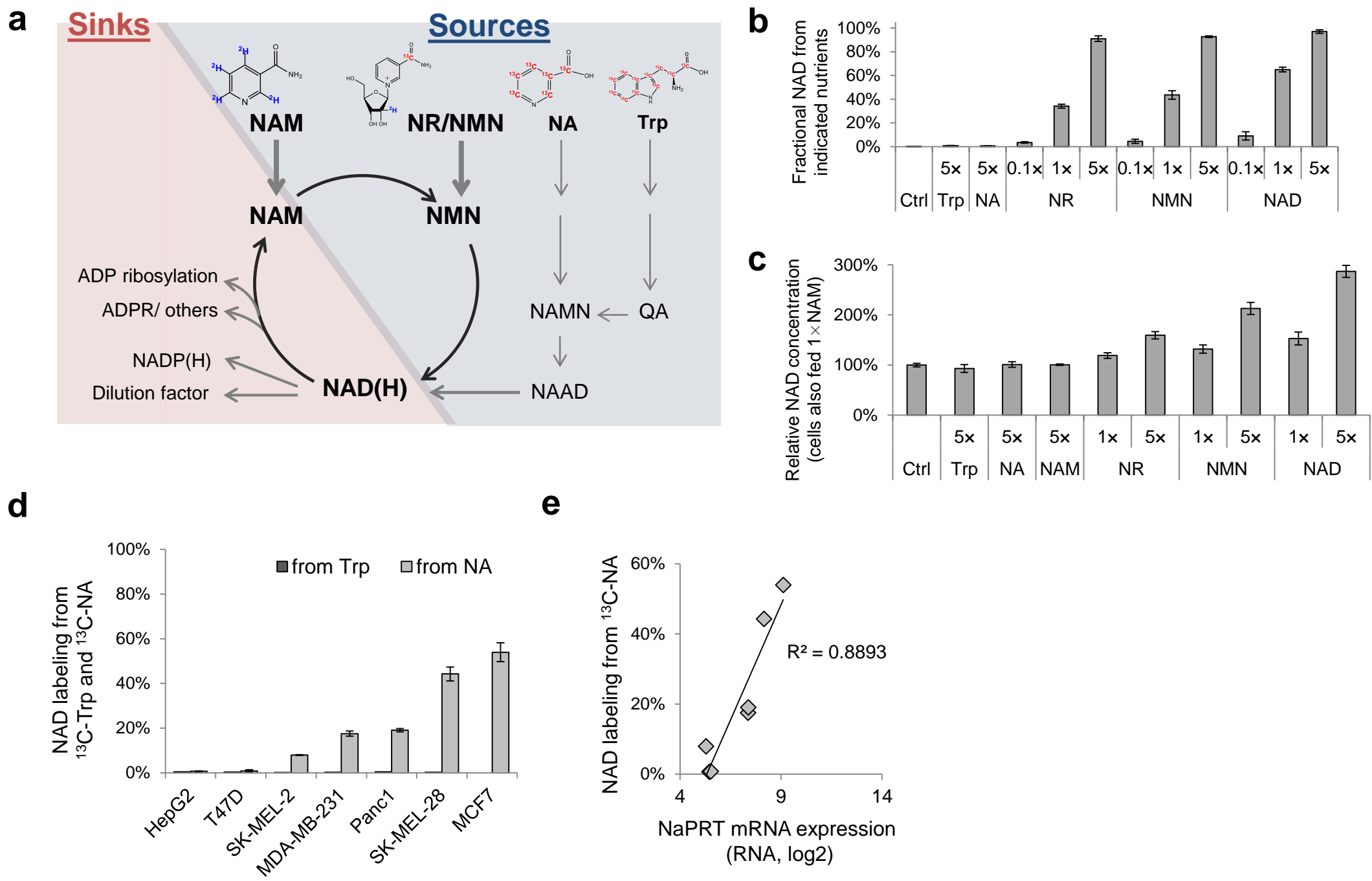
Figure S3. Contributors to NAD biosynthesis in cell lines. Related to Figure 5. **(a)** NAD biosynthesis and consumption schematic. Trp, Tryptophan; NA, nicotinic acid; NR, nicotinamide riboside; NAM, nicotinamide; NMN, nicotinamide ribotide; QA, quinolinic acid; NAAD, nicotinic acid adenine dinucleotide. **(b)** Fraction of NAD in T47D cells coming from the indicated supplemented substrate based on isotope tracing for 24 h. Compound concentrations are reported relative to nicotinamide in commercial DMEM (32 μM NAM = 1x). **(c)** NAD concentration in T47D cells fed DMEM supplemented with additional precursors for 48 h. **(d)** Labeling fraction of NAD in cells fed [U-^{13}C]Trp (5x) or [U-^{13}C]NA (1x) in DMEM for 48 h. Data are mean $\pm$ s.d., n = 3. **(e)** Across cell lines, the traction of NAD coming from NA (data from panel d) correlates with NaPRT1 mRNA expression (data from https://portals.broadinstitute.org/ccle/).
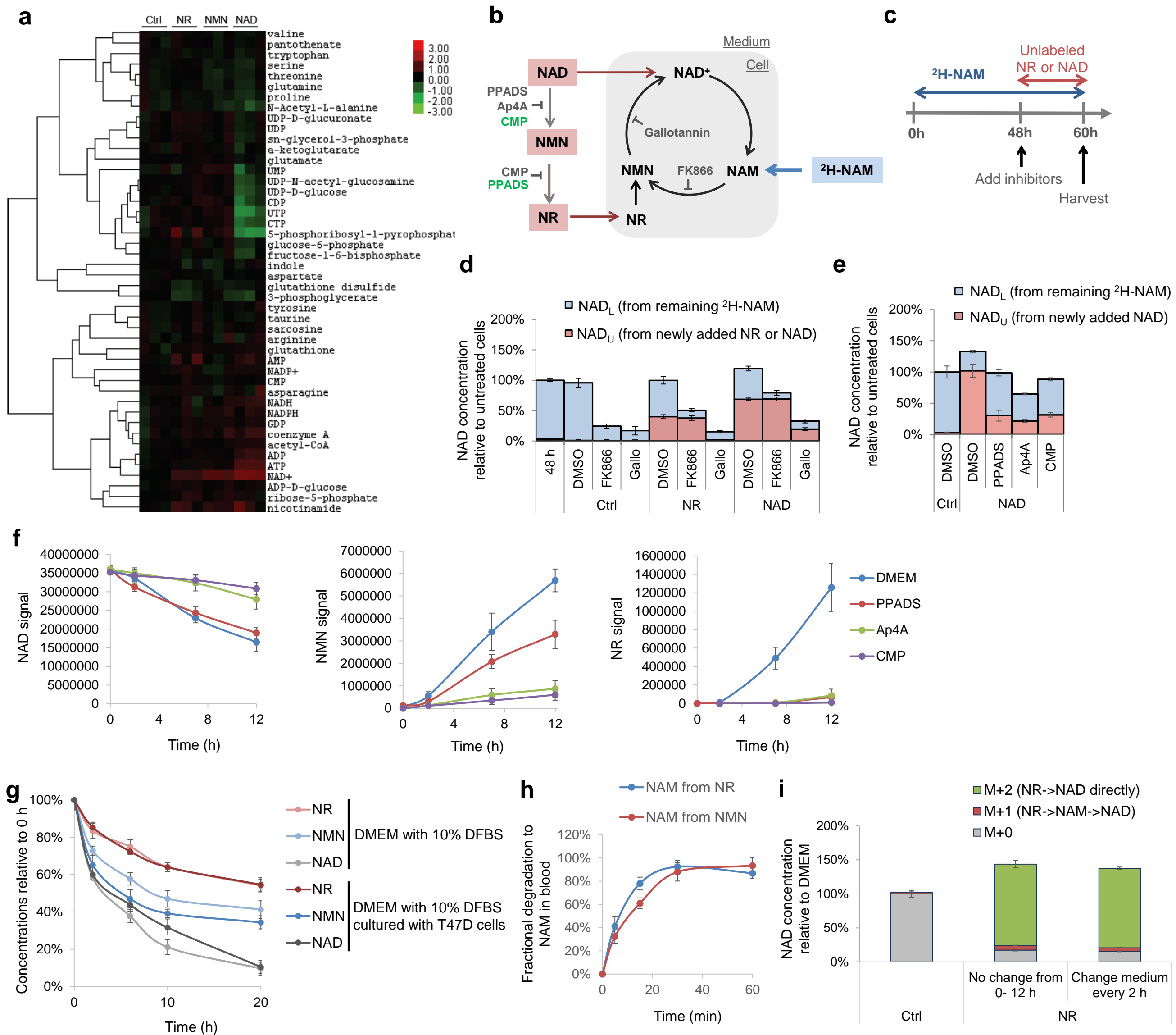
Figure S4. Metabolic impact and assimilation routes of NR, NMN, and NAD. Related to Figure 5 and Figure 7. **(a)** Heat map of metabolite concentration changes in T47D cells in response to NR, NMN, NAD (5x the concentration of NAM, individually in the presence of NAM) after 24 h. Each column represents one sample. Data were normalized to cell number. All individual samples were then normalized to the average of the control (DMEM) samples. **(b)** Schematic illustrating (i) the intracellular steps at which of gallotannin (Gallo, NMNAT inhibitor) and FK866 (NAMPT inhibitor) target NAD metabolism, (ii) the extracellular step at which Ap4A blocks the degradation of NAD to NMN, and (iii) the extracellular steps at which PPADS and CMP are expected based on literature to act (grey[38]) or were detected to act in this study (green). **(c)** Experimental design to test pathway steps required for assimilation of NR and NAD. Cells were fed ^{2}H-NAM for 48 h, after which unlabeled precursors (NAD or NR, 1x) and inhibitors (100 nM FK866, 100 μM gallotannin, 25 μM PPADS, 1 mM Ap4A or 2 mM CMP) were simultaneously added for 12 h. **(d)** NAD concentration and labeling in T47D cells with 12 h FK866 or gallotnanin treatment. Newly added NR bypassed FK866 but was blocked by gallotannin, while newly added NAD was taken intact partially and thus bypassed both steps. **(e)** NAD concentration and labeling in T47D cells treated for 12 h with PPADS, Ap4A ,or CMP. Blockade of NAD degradation by these inhibitors (as verified in panel f) partially but not fully blocked assimilation of extracellular NAD into intracellular NAD, suggesting that extracellular NAD can contribute to the intracellular NAD pool both by direct uptake and by extracellular degradation to NR followed by cellular NR uptake and metabolism. Because PPADS, Ap4A, or CMP treatment reduced unlabeled NAD by ~80%, it is likely that only a minor fraction of extracellular NAD is directly taken up by the cell, with most NAD entering the cell after its extracellular degradation. **(f)** Degradation of NAD (300 μM) into NMN and NR in fresh DMEM supplemented with 10% DFBS at 37° C, and its inhibition by PPADS, Ap4A or CMP (at the above concentrations). Unexpectedly, CMP prevented degradation of NAD to NMN, rather than exclusively blocking NMN to NR, and PPADS only modestly blocked degradation to NMN, despite preventing the appearance of NR. **(g)** Stability of 100 μM NR, NMN and NAD in DMEM supplemented with 10% DFBS (37° C), and in DMEM with 10% DFBS cultured with T47D cells. Concentrations were normalized to 0 h. **(h)** Degradation of NR and NMN into NAM in blood at 37° C. NAM concentrations were normalized to the added NR and NMN concentration (100 μM). **(i)** NAD concentration in T47D cells fed ^{2}H,^{13}C-NR (5x, 32μM=1x) for 12 h. Medium was either refleshed every 2 h, or remained unchanged. Data are mean ± s.d., n = 3. Lines are to guide the eye.
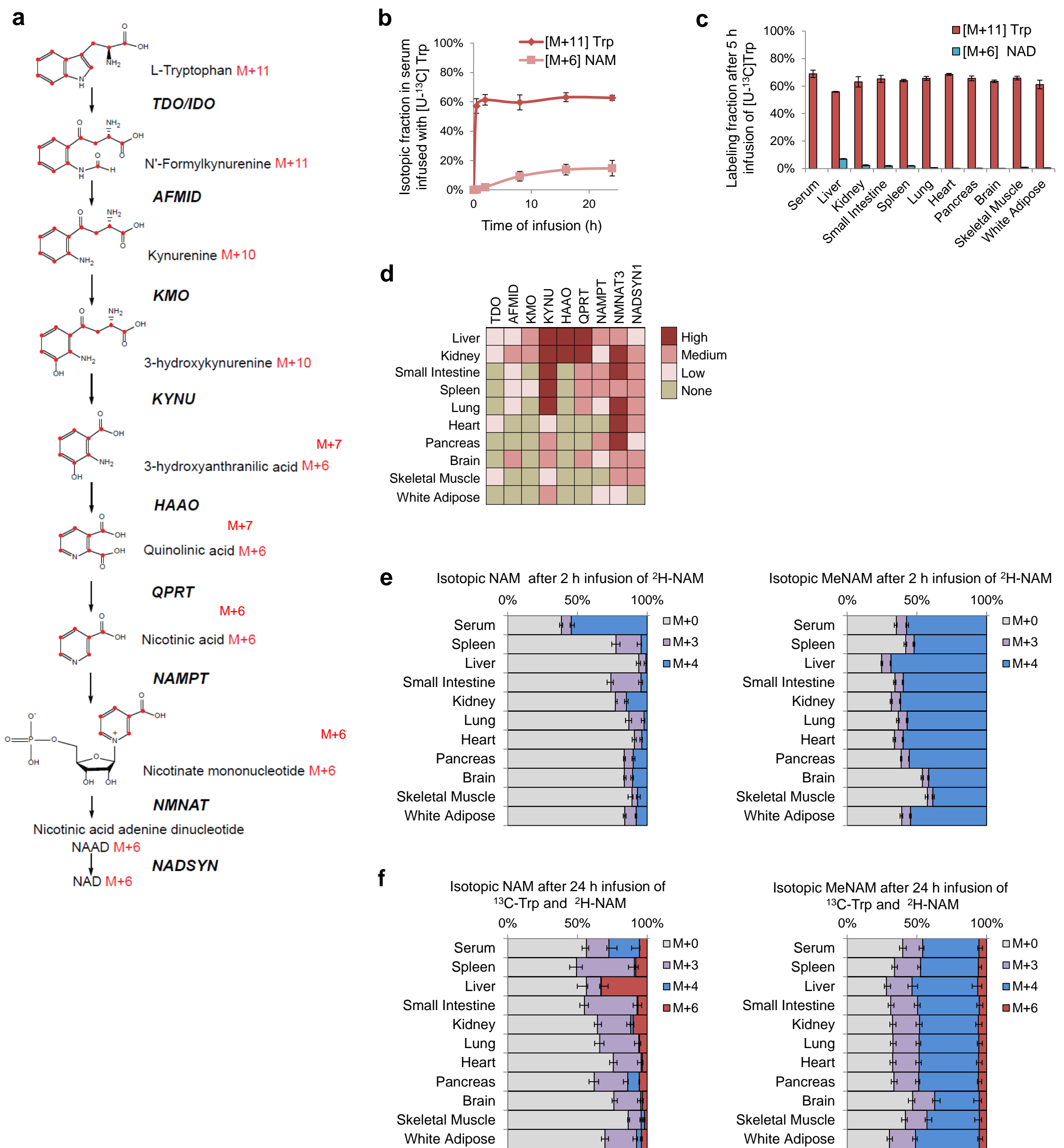
Figure S5. *De novo* NAD synthesis, and labeling of NAM and N-methylnicotinamide (MeNAM). Related to Figure 5. **(a)** *De novo* pathway with labeling states of intermediates from [U-^{13}C]Trp indicated. **(b)** Isotopic fractions of tryptophan and NAM in serum. ^{13}C-Trp was infused via jugular vein at 5 nmol/g/min. Lines are to guide the eye. **(c)** Labeled fractions of tryptophan and NAD in tissues after 5 h [U-^{13}C]Trp infusion. Note that NAD labeling is greatest in liver. Data are mean ± s.d., n=3. **(d)** Liver and kidney have the complete set of NAD *de novo* synthesis enzymes. Data are from the Human Protein Atlas. **(e-f)** NAM and MeNAM labeling in serum and tissues. MeNAM displayed similar labeling across tissues, indicating rapid sharing of MeNAM (unlike NAM itself) throughout the body via the circulation. Mice were either infused with ^{2}H-NAM for 2 h **(e)**, or co-infused with ^{2}H-NAM and ^{13}C-Trp for 24 h **(f)**. Data are mean ± s.d., n=2.
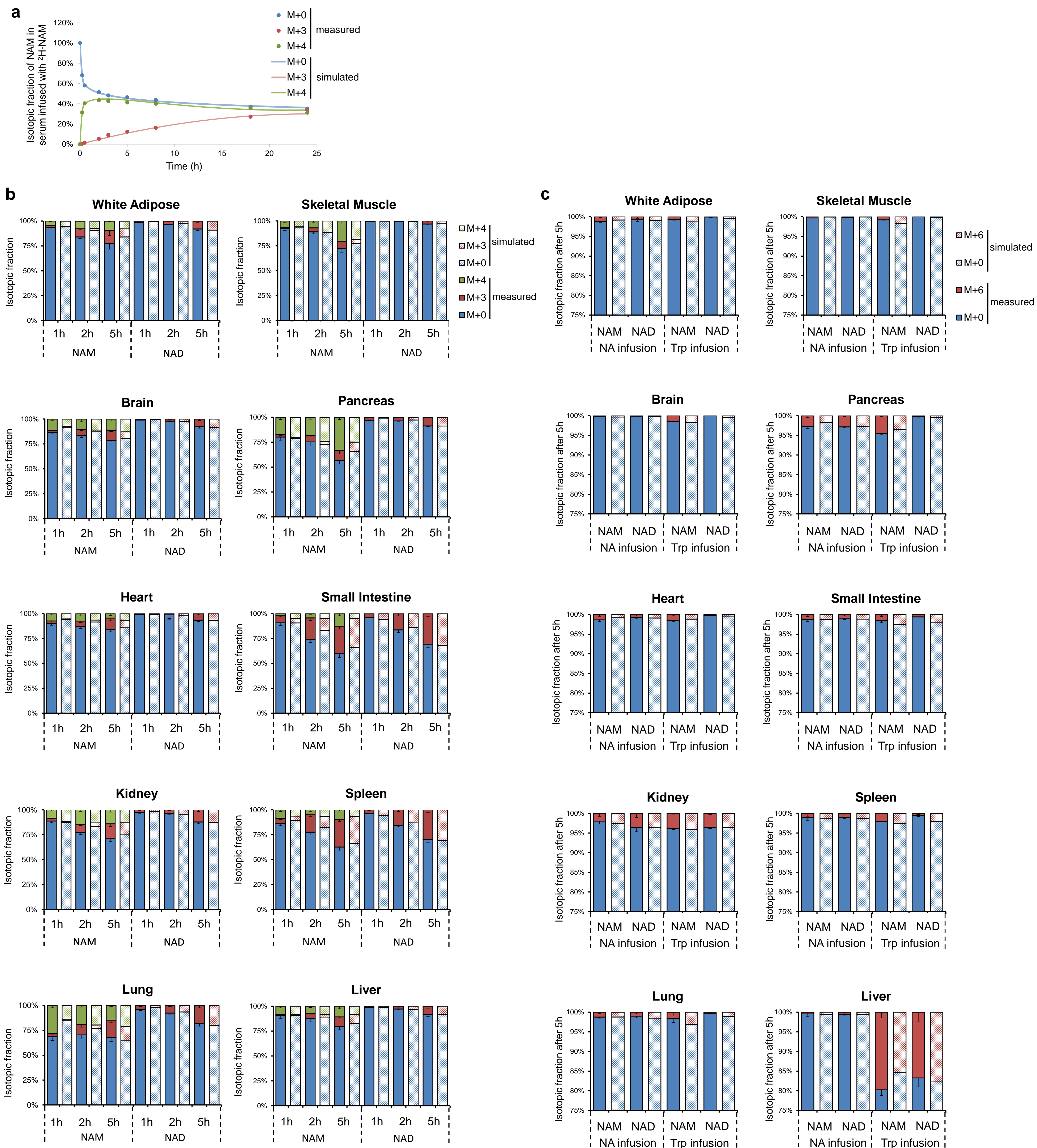
Figure S6. The goodness of fit of NAM and NAD labeling data. Related to Figure 6. **(a)** Experimentally measured (dots) and polynomial interpolated (lines) serum NAM labeling fractions are compared. For $NAM_{[M+0],t} = 1.7533t^2 - 1.7139t + 1$ [0,0.5], $-0.059\ln(t) + 0.5489$ [0.5,24]; $NAM_{[M+3],t} = -0.0005t^2 + 0.0245t$; $NAM_{[M+4],t} = 1- NAM_{[M+0],t} - NAM_{[M+3],t}$. **(b)** Across 10 tissues, measured and simulated NAM and NAD isotopic labeling fractions from [2,4,5,6-^{2}H]NAM infusion are compared. **(c)** Analogous results for [U-^{13}C]Trp and [U-^{13}C]NA infusions.
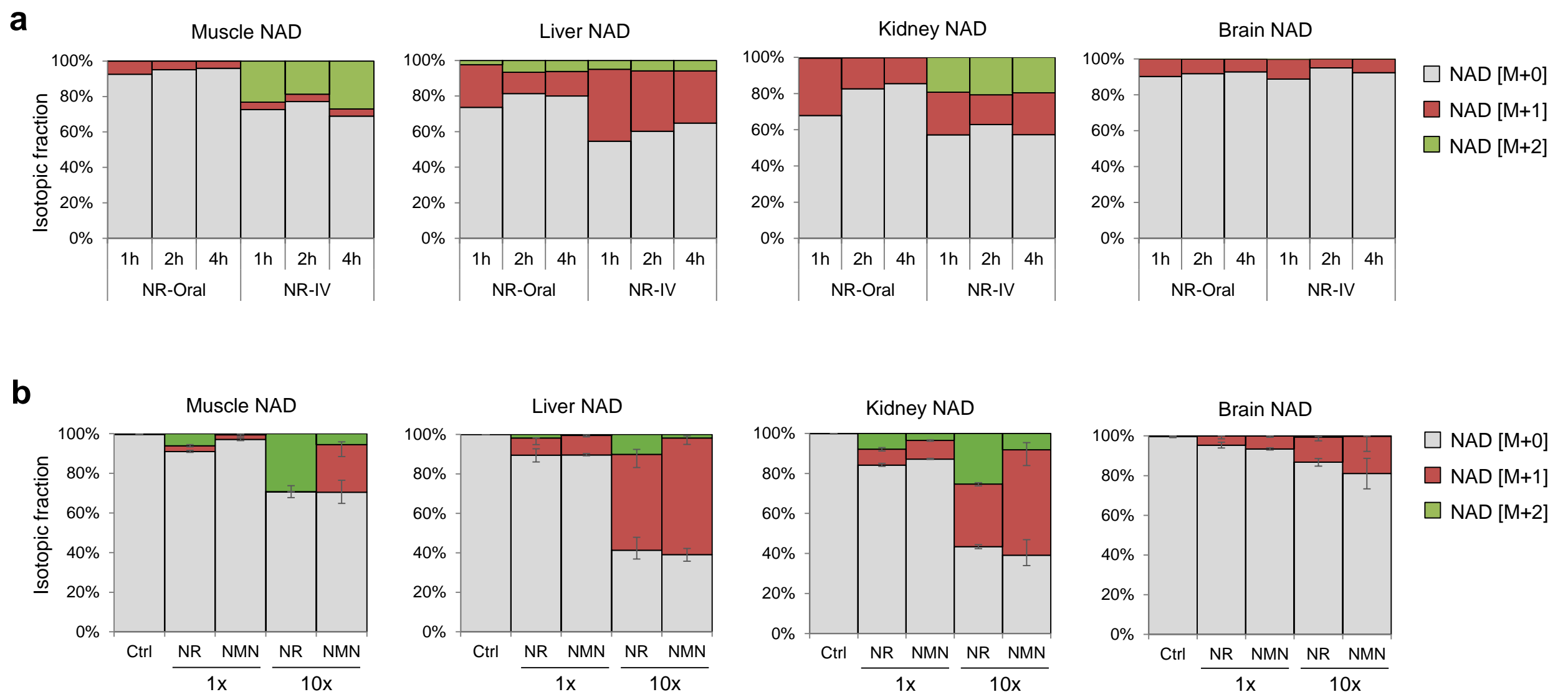
Figure S7. Metabolism of high dose NR and NMN. Related to Figure 7. **(a)** Tissue NAD labeling, at the indicated times after a 200 mg/kg bolus (4x) of ^{2}H,^{13}C-NR by oral gavage or by IV injection (n=1 per time point). **(b)** Tissue NAD labeling after 2 h of either 50 mg/kg (1x) or 500 mg/kg (10x) bolus of ^{2}H,^{13}C-NR or ^{2}H,^{13}C-NMN by IV injection. Data are mean ± s.d., n=3 for 50 mg/kg (1x), n=5 for 500 mg/kg (10x).